Energy Transfer and Scale Dynamics in 2D and 3D Laser Driven Jets

H. Yin,[1,2] J. K. Shang,[1,2,3] E. G. Blackman,[4,2,3] G. W. Collins,[1,2,3] and H. Aluie[1,2,3]
[1)]*Department of Mechanical Engineering, University of Rochester, Rochester, NY 14627, USA*
[2)]*Center for Matter at Atomic Pressures, University of Rochester, Rochester, NY 14627, USA*
[3)]*Laboratory of Laser Energetics, University of Rochester, Rochester, NY 14623, USA*
[4)]*Department of Physics and Astronomy, University of Rochester, NY 14627, USA*

(*Electronic mail: hussein@rochester.edu)

(*Electronic mail: j.k.shang@rochester.edu)

(Dated: 31 August 2023)

We demonstrate a methodology for diagnosing the multiscale dynamics and energy transfer in complex HED flows with realistic driving and boundary conditions. The approach separates incompressible, compressible, and baropycnal contributions to energy scale-transfer and quantifies the direction of these transfers in (generalized) wavenumber space. We use this to compare the kinetic energy (KE) transfer across scales in simulations of 2D axisymmetric versus fully 3D laser driven plasma jets. Using the FLASH code, we model a turbulent jet ablated from an aluminum cone target in the configuration outlined by Liao *et al.* [A. S. Liao, S. Li, H. Li, K. Flippo, D. Barnak, K. V. Kelso, C. Fiedler Kawaguchi, A. Rasmus, S. Klein, J. Levesque, C. Kuranz, and C. Li, Physics of Plasmas, 26, 032306 (2019)]. We show that, in addition to its well known bias for underestimating hydrodynamic instability growth, 2D modeling suffers from significant spurious energization of the bulk flow by a turbulent upscale cascade. In 2D, this arises as vorticity and strain from instabilities near the jet's leading edge transfer KE upscale, sustaining a coherent circulation that helps propel the axisymmetric jet farther ($\approx 25\%$ by 3.5 ns) and helps keep it collimated. In 3D, the coherent circulation and upscale KE transfer are absent. The methodology presented here may also help with inter-model comparison and validation, including future modeling efforts to alleviate some of the 2D hydrodynamic artefacts highlighted in this study.

I. INTRODUCTION

High speed jets arise in many astrophysical and high energy density (HED) applications[1]. In astrophysics, supersonic hydrodynamic jets can arise as an initially collimated outflow or an otherwise quasi-spherical supersonic blast wave propagating into an inhomogeneous medium. Jets appear on sources of all scales of astrophysics, including supernovae evolution[2]. In inertial confinement fusion (ICF), jets result from the interaction between a shock and density perturbations such as those due to the fill-tube[3] or due to voids[4,5]. These jets can trigger the mixing of ablator and fuel, which ultimately degrade the ignition yield[6,7]. Jets can often be characterized as complex multi-scale flows involving instabilities and turbulence, and in many cases, instabilities trigger turbulent mixing[8,9].

Turbulence is common in complex HED flows in astrophysics and ICF. In the evolution of core-collapse supernovae for example, turbulence is generated due to instabilities between the inner core and the outgoing shock[10–12]. Energy transfer between scales is believed to play a key role in such simulations and may account for differences between 2D and 3D[13–15]. In particular, it is believed that upscale (inverse) transfer of kinetic energy in 2D may help to increase the efficacy of turbulent transport of heat to the shock to prevent it from stalling, making explosions easier to achieve than in 3D.

Instabilities are also common in complex HED flows in astrophysics and ICF. For example, the Rayleigh-Taylor (RT) instability in ICF has been a significant hindrance to ignition[16]. In ICF, 2D simulations are the main "work horse" for experimental design[17–19] as routine 3D simulations are prohibitively expensive. A capsule-only 3D simulation requires tens to hundreds of millions of CPU hours on supercomputers even without incorporating the hohlraum and laser physics[20,21]. The trade-offs between 2D and 3D flow physics are still not widely appreciated in ICF simulations. The primary objective of this study is to highlight the differences in energy scale-transfer how they affect the travel of laser-driven jets between 2D and 3D.

Length scales in complex flows are generally characterized by a wavenumber energy spectrum. Yet the energy transfer pathways and interactions between different scales are often subtle and cannot be diagnosed using the spectrum alone. In this work, we investigate two processes that transfer energy across scales: deformation work, Π, and baropycnal work, Λ.

Deformation work is due to the multi-scale nature of the velocity field and is the sole mechanism for energy transfer across scales (or cascade) in constant-density (incompressible) flows described by the Navier-Stokes equation[22,23]. In 3D incompressible homogeneous turbulence, the main mechanism behind Π is believed to be vortex stretching[24–28], which transfers energy downscale. Kraichnan[29] predicted and subsequent studies[30,31] have demonstrated that an incompressible homogeneous turbulent flow, when restricted to two spatial dimensions, will tend to transfer energy in the opposite direction, *i.e.*, upscale rather than downscale, due to vorticity conservation in 2D. However, HED flows involve significant density variations and do not conserve vorticity, even when restricted to 2D, due to baroclinicity. Therefore, extending such phenomenologies[29,31] from incompressible homogeneous flows to inhomogeneous flows with variable density remains dubious[32]. A main contribution in this work is to demonstrate, via a direct measurement of Π, that an upscale

cascade can indeed arise in 2D hydrodynamic models of HED systems, despite the lack of vorticity conservation.

The second energy transfer pathway we analyze here is baropycnal work Λ, which results from pressure and density variations at different scales[33,34]. The direction of energy transfer by Λ depends on the source of pressure gradient and density variations[32,35–38]. Typical cases include (i) a baroclinic flow wherein Λ transfers energy downscale into small-scale velocity fluctuations due to opposing directions of pressure and density gradients[32], and (ii) a shock wherein pressure and density gradients are aligned and Λ transfers energy upscale into the large-scale pressure field[34,36,38].

Previous works have utilized coarse-graining methods that are common in Large Eddy Simulation modeling[39] to decompose length scales and analyze deformation work[40,41] and baropycnal work[33,38,42]. Lees & Aluie[42] conducted simulations of compressible turbulence in 3D with varying levels of compressibility. Their results demonstrated that in 3D homogeneous compressible turbulence, Π transfers energy downscale to the small-scale turbulence while Λ transfers energy upscale into large-scale potential energy residing in the pressure field. Zhao *et al.*[32] analyzed the energy scale-transfer in baroclinically unstable flows by simulating the RT instability and the ensuing late-stage turbulence in 2D and 3D. They found that in both 2D and 3D, Λ transfers energy downscale by releasing potential energy stored at the largest scales and depositing it over a wide range of smaller scales in the fully turbulent regime. Energy transfer by Π, on the other hand, exhibits opposing behaviors in 2D versus 3D[32]. In 2D, upscale transfer by Π leads to higher bulk kinetic energy at large scales, whereas in 3D, the energy transfer is downscale.

Here, we extend and demonstrate the methodology to high energy density (HED) flow regimes by taking advantage of laser-driven jets. We reference the simulation configuration by Liao *et al.*[43], which proposes a design to set up a turbulent dynamo operating on the OMEGA-EP laser[44,45]. This design, sketched in Fig. 1, shines multiple laser beams on the inner wall of a cone target to create a supersonic turbulent jet. In section II, we describe the model configurations, address the sensitivity to initial conditions in 2D and 3D, and report on the jets' evolution and properties. In section III, we introduce the coarse-graining method for scale decomposition and define the energy scale-transfer terms, Π and Λ. In section IV, we analyze KE at large scales and show that the corresponding difference between 2D and 3D can be quantified by Π and Λ. In section V, we characterize the turbulent region at the jet's leading edge using subscale stress and discuss KE scale-transfer in that region. In section VI, we decompose Π and Λ into contributions from the divergence-free and irrotational components of the flow to examine the mechanism causing the 2D jet's leading edge to remain narrow. We summarize the results in the concluding section VII.

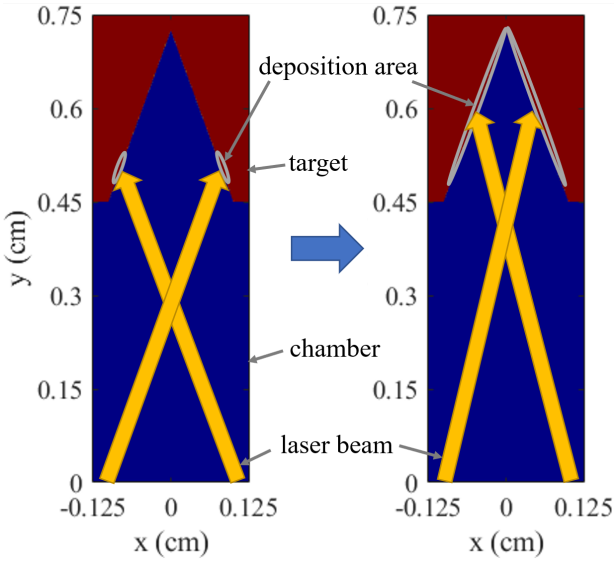

FIG. 1. Configuration of run (left) L5R090 and run (right) L6R720. Label "L" denotes the location of laser deposition along the y-direction (in millimeters) and label "R" denotes the radius of the laser beam (in micrometers). Note that the deposition area is larger than the beam size since the laser propagation direction is not perpendicular to the cone surface.

II. NUMERICAL SIMULATIONS

A. Simulation Configurations

FLASH is a multiphysics radiation-hydrodynamics code used frequently for HED applications. It provides a comprehensive environment for full-physics laser driven simulations by solving governing equations in three-temperature unsplit hydrodynamics on an adaptive mesh refinement (AMR) grid[46,47]. The laser driven simulation module includes features of laser ray tracing[48], electron thermal conduction with Spitzer conductivities[49], and radiation diffusion with tabulated opacity[50]. Liao *et al.*[43] used the FLASH code to develop a test platform for laser-driven turbulent dynamos that matches realizable OMEGA-EP experimental configurations in 3D[43]. We conduct our 3D simulations using a similar configuration that generates turbulence by the interaction of laser ablated jets. To simulate the analogous cone target in 2D, we employ cylindrical coordinates, which significantly modifies the configuration of Liao *et al.* in that the laser deposition becomes azimuthally symmetric. To approximate this modification in 3D, within Cartesian coordinates, we simulate a quasi-azimuthally symmetric configuration in which 256 laser beams deposit energy symmetrically about the center vertical axis of the target. We investigate sensitivity to the laser drive and show the validity of comparing 2D and 3D simulations below. In both 2D and 3D geometries, UV laser beams (351 nm wavelength) deliver a total power of 0.5 TW over a 3.5 ns duration using square pulses. The simulations use multigroup diffusion for radiation transport using 6 groups.

As shown in Fig. 1 the simulation domain is 0.25 cm wide

and 0.75 cm high, and the target occupies 0.3 cm of height from the top boundary of the domain. The main target is 2.7 g/cc aluminum notched into a hollow cone with an interior space of 0.2 cm diameter at the cone base and 0.274 cm of height filled with a pseudo-vacuum of 10^{-6} g/cc helium. The vacuum region extends from the cone's opening to the bottom of the domain over 0.45 cm. The equations of state (EOS) and opacity of both the aluminum cone and helium pseudo-vacuum are obtained from the atomic database IONMIX[51].

Due to the nature of cylindrical coordinates, the 2D computational domain takes an axisymmetric boundary at $x = 0$ in Fig. 1 as the center axis, for which both normal and toroidal vector components change sign. The boundaries everywhere else are outflow, which specifies a zero gradient to allow the flow to leave the domain freely. The 3D computational domain takes outflow boundaries in all directions. In this work, all visualizations of the 2D domain are mirrored about the axisymmetric boundary ($x = 0$) to compare to the slice of the 3D domain.

Applying adaptive mesh refinement[52], we set the initial static grid size of a mesh block to be 16 in all directions, with a maximum refinement level of 5 in both 2D and 3D. Each refinement level doubles the grid size at the finest resolution. Since the computational domain's aspect ratio is 1:6 in 2D and 1:3 in 3D, we use 3 mesh blocks in 3D aligned in the vertical direction and 6 mesh blocks in 2D. The effective mesh resolution can be calculated as $(grid\ size\ of\ single\ block) \times 2^{(max\ refinement\ level-1)} \times (number\ of\ blocks)$, which gives the resolution 256×1536 in 2D and $256 \times 256 \times 768$ in 3D. The mesh refinement criterion used is the modified Löhner's estimator[50], for which we set the density and electron temperature to be the refinement variables and the threshold value to trigger refinement is 0.8. This grid mesh configuration resolves turbulence structures that appear around the leading edge of the jet at late times. In the Appendix, we report on our analysis of numerical convergence (see Fig. 20).

B. Sensitivity to Laser Drive

Fig. 1 shows initial configurations for runs L5R090 and L6R720, where the label "L" denotes the y-location of laser deposition in millimeters and the label "R" is the radius of laser deposition in microns. Due to the inherent azimuthal symmetry in the 2D simulations, which requires only one laser beam to illuminate the entire target. In 3D, the beams are separated with equal angle azimuthally on the cone. Matching the 2D and 3D configurations of the initial flow is crucial for making comparisons. Here, we list a few laser-drive parameters that play an important role in the initial flow's development.

First, the number of laser rays traced in the simulation significantly affects the ablated flow's smoothness at early times. As shown in Figs. 2a, 2c, the same number of rays reveals distinct early-time velocity profile differences. The 2D initial flow using 4096 rays in the single beam manifests large-scale non-uniformity in the reflected-energy region ($y > 0.5325$ cm, highlighted by arrows in Fig. 2), whereas this issue is absent in 3D due to using a higher number of laser beams, each with 4096 rays. With a sufficient number of rays shown in Fig. 2b, the early-time velocity profile off the ablated surface agrees in 2D and 3D.

TABLE I. Kinetic energy (KE) and internal energy (IE) per volume (in erg/cm^3) in different regions of the domain at $t = 0.3$ ns.

Run	KE^{up}(y>0.5325 cm)	KE^{down}(y<0.5325 cm)	KE^{tot}	$KE^{tot}+IE^{tot}$	KE^{up}/KE^{tot}
2D L5R090	2.27×10^{7}	2.96×10^{8}	3.19×10^{8}	1.26×10^{9}	7%
3D L5R090	6.12×10^{6}	2.42×10^{8}	2.48×10^{8}	1.26×10^{9}	2%
2D L6R720	7.58×10^{7}	1.70×10^{8}	2.46×10^{8}	1.29×10^{9}	31%
3D L6R720	5.82×10^{7}	1.27×10^{8}	1.85×10^{8}	1.29×10^{9}	31%

Second, the radius of laser deposition has an important role in matching the early-time evolution in 2D and 3D. In run L5R090, the reflected laser energy appears in the domain at $y > 0.5325$ cm in Fig. 2, highlighted by white arrows. However, the fraction of reflected energy differs between 2D and 3D, which leads to differences in the mass ablated at different locations along the cone surface. This can be quantified by comparing the kinetic energy at $y > 0.5325$ cm, KE^{up} to kinetic energy over the entire domain, KE^{tot}. Their ratio, KE^{up}/KE^{tot}, is listed in Table I and shows a mismatch between 2D and 3D for run L5R090. Using a larger radius for the laser deposition area minimizes ablation from reflected radiation and, therefore, minimizes differences between 2D and 3D in the early-time flow. This is achieved in run L6R720 in Fig. 3, where the fraction KE^{up}/KE^{tot} is the same in 2D and 3D in Table I. Since the y-momentum, G_y, is central to the jet's traveling distance, we also show a similar ratio G_y^{up}/G_y^{tot} in Table II, which agrees between 2D and 3D in run L6R720. Despite increasing the laser radius in run L6R720, it is still necessary to use a sufficient number of rays in 2D to match the early-time solutions from the 2D and 3D simulations, as discussed in the previous paragraph.

Third, to create quasi-azimuthally symmetric laser deposition in 3D, we increase the number of laser beams until the traveling distance of the jet converges. This is characterized by the y-momentum centroid along the y-direction,

$$G_y^{centroid} = \frac{\int dV\ \rho u_y y}{\int dV\ \rho u_y}, \tag{1}$$

where u_y is the y-component of velocity, ρ is mass density, and V is the volume of the physical domain. As shown in Fig. 4, run L5.5R360 in 3D converges using 128 laser beams while L6R720, which uses a larger beam radius, requires only 64 beams. A larger beam radius makes it easier to approximate azimuthal symmetry with fewer beams as expected. Considering the three factors discussed above, we use run L6R720 in the rest of the paper.

Fig. 5 uses run L6R720 to demonstrate that kinetic energy is almost identical between 2D and 3D, differing by 0.47% at $t = 3.5$. Fig. 5 plots kinetic energy KE, internal energy IE, and the total energy E^{tot} being the sum of the KE and IE. Internal energy is also almost identical between 2D and 3D, differing by 2.1% at $t = 3.5$ ns. To quantify the similarity between 3D quasi-azimuthal symmetry and 2D azimuthal symmetry, we take the standard deviation of the averaged kinetic energy

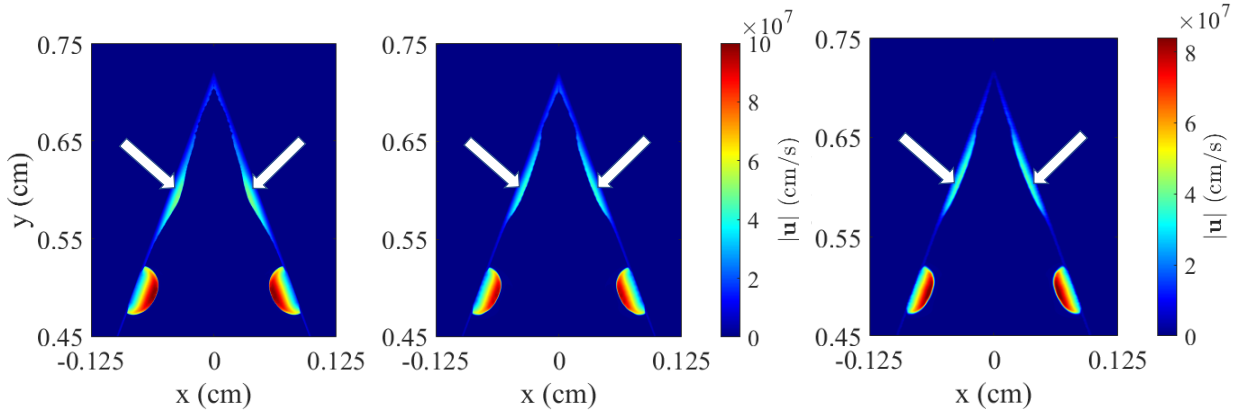

(a) 2D - 4096 rays per beam (b) 2D - 32768 rays per beam (c) 3D - 4096 rays per beam ×256 beams

FIG. 2. The number of laser rays affects the ablated flow's smoothness. Panels show velocity magnitude from run L5R090 at $t = 0.3$ ns and $y > 0.45$ cm using different numbers of laser rays. Even though the laser beams are incident on the cone in the region around $y = 0.5$ cm, a fraction of this laser energy is reflected deeper into the cone around $y = 0.6$ cm highlighted by the white arrows in the panels. This reflected laser energy induces a flow, which is sensitive to the number laser rays. Comparing panels (a) and (b), we can see that using 4096 rays in the single beam in 2D manifests large-scale non-uniformity in the ablated flow. With 32768 rays in the single beam in 2D in panel (b), the velocity profile off the ablated surface agrees with 3D in panel (c), which uses 4096 rays/beam ×256 beams. Panel (c) is a slice in the 3D domain at $z = 0$ cm.

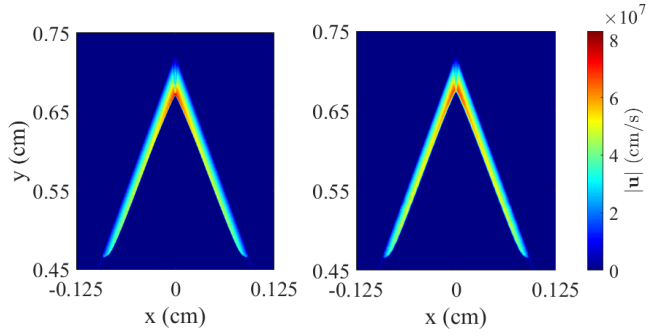

(a) 2D (b) 3D

FIG. 3. A wider laser beam helps match the early-time evolution in 2D and 3D. Panels show velocity magnitude from run L6R720 at $t = 0.3$ ns and $y > 0.45$ cm using a laser beam that is wider than that in L5R090 shown in Fig. 2 (b)-(c). Panel (b) is a slice in the 3D domain at $z = 0$ cm.

TABLE II. Axial y-momentum per volume (in g cm/s/cm^3) in different regions of the domain at $t = 0.3$ ns.

Run	G_y^{up}(y>0.5325 cm)	G_y^{down}(y<0.5325 cm)	G_y^{tot}	G_y^{up}/G_y^{tot}
2D L5R090	4.90	16.69	21.58	23%
3D L5R090	2.10	14.84	16.94	12%
2D L6R720	8.89	16.86	25.75	35%
3D L6R720	6.29	12.71	19.01	33%

along the azimuthal direction,

$$\langle KE\rangle_\theta^{std} = \sqrt{\frac{\sum_{i=1}^{N}(\langle KE\rangle_{\theta_i} - \overline{\langle KE\rangle}_\theta)^2}{N-1}}, \qquad (2)$$

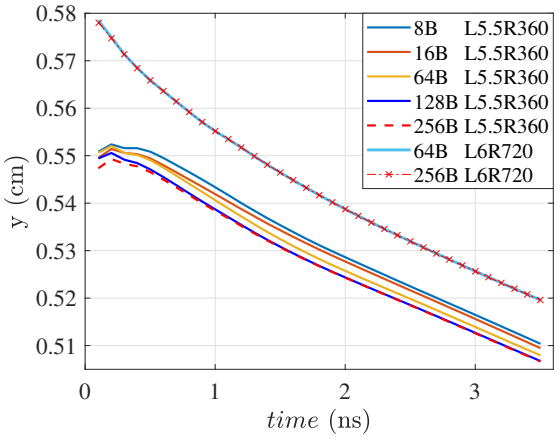

FIG. 4. To create quasi-azimuthally symmetric laser deposition in 3D requires a sufficiently large number of overlapping laser beams. Convergence of jet's traveled distance as a function laser beam number is quantified by the y-momentum centroid, $G_y^{centroid}$, in eq. (1). This is plotted here using an increasing number of laser beams labeled with "B". Runs L5.5R360 converges with 128 laser beams and runs L6R720 converges with only 64 laser beams due to a wider beam radius.

where θ is the azimuthal angle, $\langle ...\rangle_\theta$ is the domain average at an azimuthal coordinate, N is the number of θ bins and the overbar denotes the average over all θ. We find a percentage of 2.9% by comparing $\langle KE\rangle_\theta^{std}$ to the domain averaged kinetic energy, $\langle KE\rangle$, at $t = 3.5$ ns in 3D. This percentage quantifies the $\langle KE\rangle$ variance in the azimuthal direction. Naturally, this variance is identically 0% for the 2D simulation.

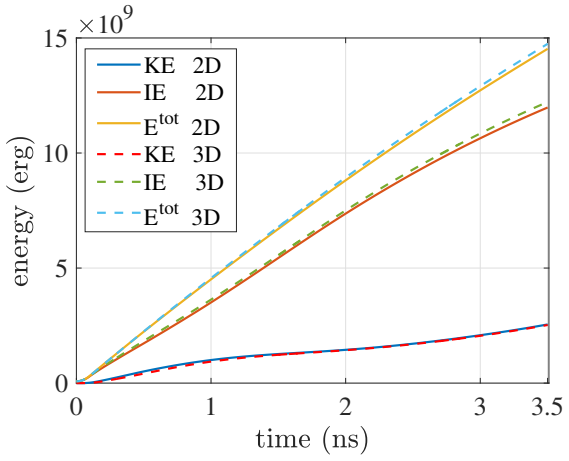

FIG. 5. Comparison of kinetic energy (KE), internal energy (IE) and total energy (E^{tot}) between 2D and 3D from run L6R720. KE in 2D and 3D are almost identical with difference of only 0.47% at $t = 3.5$ ns.

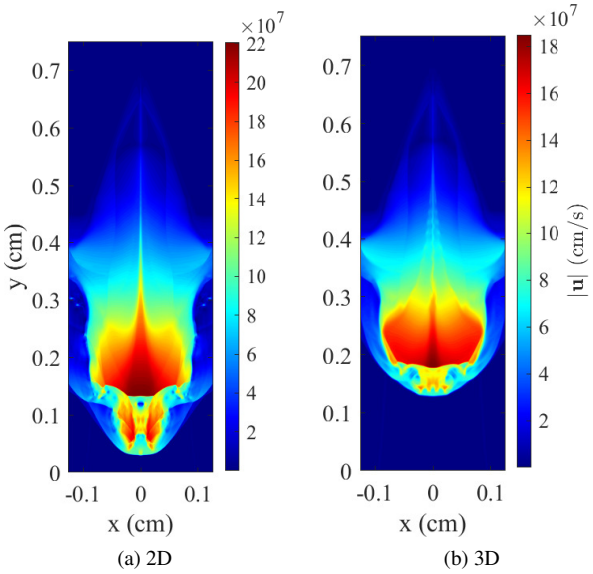

FIG. 6. Visualization of velocity magnitude, $|\mathbf{u}|$, from run L6R720 at $t = 3.5$ ns. Despite having almost identical domain-integrated kinetic energy in 2D and 3D, the jet travels a longer distance in 2D than in 3D. This indicates that KE resides at different scales between the two configurations, which is most evident at the leading edge of the jets. Panel (b) is a slice in the 3D domain at $z = 0$ cm.

C. Jet Traveling Distance

All visualizations in the remainder of this paper are shown from run L6R720 at time $t = 3.5$ ns, which is approximately when the jet reaches the bottom of the domain and are shown at the cross section in xy-plane at $z = 0$. In Fig. 6, the jet exhibits turbulent structures in both 2D and 3D, especially at the leading edge, which we characterize using the subscale stress discussed in Section V. It is evident from the velocity profiles

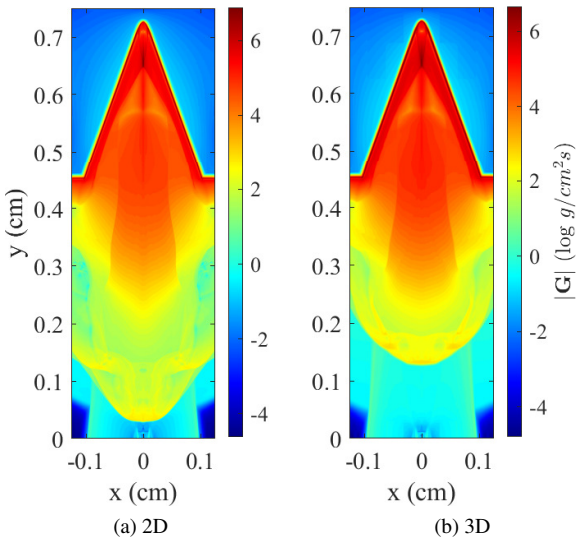

FIG. 7. To complement Fig. 6, this figure visualizes momentum magnitude, $|\mathbf{G}| = |\rho\mathbf{u}|$, at $t = 3.5$ ns (note the log-scale colorbar). Momentum at the leading edge of the jet is a few orders of magnitude smaller relative to that near the cone's surface, which underscores the wide variations in density.

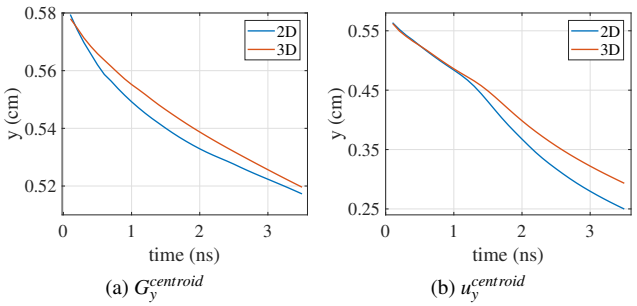

FIG. 8. Distance traveled by the jet along the y-axis, characterized by (a) the y-momentum centroid, $G_y^{centroid}$, and (b) y-velocity centroid, $u_y^{centroid}$. Comparing 2D and 3D at $t = 3.5$ ns, $G_y^{centroid}$ differs by 6.8% and $u_y^{centroid}$ differs by 16.1%.

in Fig. 6 that the jet travels farther in 2D than 3D, despite having almost identical domain-integrated kinetic energy (Fig. 5). This indicates that KE resides at different scales between the two configurations, which is most evident at the leading edge of the jets. A shock that is reflected from the jet's leading edge, traveling toward the cone, can be seen as a discontinuity in the velocity at $y \approx 0.15$ to 0.2 cm in Fig. 6 (see also Fig. 2 in Ref.[53]).

To objectively compare the 2D and 3D jets we use the y-momentum centroid in the y-direction in eq. (1). This metric gives a bulk characterization of the jet's movement. A momentum-based metric is more appropriate than a center of mass, which would include low-velocity material near the cone. Fig. 8a plots the traveling distance in time and shows

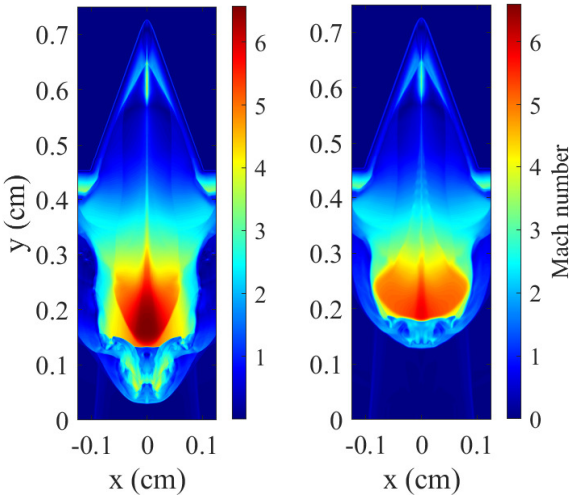

(a) 2D (b) 3D

FIG. 9. Visualization of Mach number, $M = |\mathbf{u}|/c$, at $t = 3.5$ ns. Here, c is the local sound speed. Higher values of M in 2D indicates higher levels of compressibility relative to 3D.

that the jet in 2D travels farther than 3D at all times. Another metric we use is the y-velocity centroid in the y-direction,

$$u_y^{centroid} = \frac{\int dV\ u_y y}{\int dV\ u_y}, \tag{3}$$

to highlight the discrepancy seen in Fig. 6. Plots of $u_y^{centroid}$ in Fig. 8b show a consistent message that the jet in 2D travels farther than 3D at all times, with a difference of 16.1% at $t = 3.5$ ns. Differences based on $u_y^{centroid}$ are larger than those based on $G_y^{centroid}$ since density at the leading edge is a few orders of magnitude smaller compared to the region near the target. This can be gleaned from comparing Figs. 6,7. A third metric we use is based on identifying the position of the leading edge, $\rho_y^{leading}$, which we define as the location where density jumps by a factor of 100. We find that leading edge in 2D has traveled 26.7% farther than in 3D at $t = 3.5$ ns.

D. Compressibility Metrics

For completeness, we report on the compressibility levels of the flow using two quantities. First, in Fig. 9, we show the pointwise Mach number, $M = |\mathbf{u}|/c$, where $|\mathbf{u}|$ is magnitude of the local velocity in the lab frame and c is the local sound speed. The Mach number in 2D is generally greater than in 3D, especially in the pre-shocked region at $y \approx 0.15$–0.3 cm, which is consistent with the 2D jet being generally faster than in 3D. To quantify the differences in Fig. 9, we show the bulk Mach number, $M = \langle|\mathbf{u}|\rangle/\langle c\rangle$, in Appendix Fig. 21a where $\langle\ldots\rangle$ is the domain average. A difference of 12.1% between 2D and 3D occurs at the end of the simulation ($t = 3.5$ ns).

Second, in Fig. 10, we calculate the time series of $|\nabla\cdot\mathbf{u}|_{rms}$ and $|\nabla\times\mathbf{u}|_{rms}$, which are more sensitive to the flow at smaller

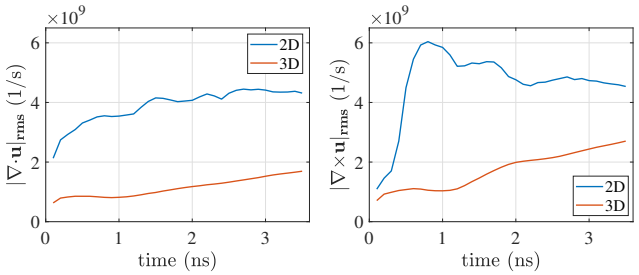

(a) $|\nabla\cdot\mathbf{u}|_{rms}$ (b) $|\nabla\times\mathbf{u}|_{rms}$

FIG. 10. Root mean square (rms) of (a) divergence of velocity and (b) vorticity. Ratio $|\nabla\cdot\mathbf{u}|_{rms}/|\nabla\times\mathbf{u}|_{rms}$ characterizes compressibility levels at small scales. In panel (b), the vortical component at small scales decreases in 2D due to upscale energy transfer as we discuss in Section VI below.

scales due to shocks and turbulence. Both $|\nabla\cdot\mathbf{u}|_{rms}$ and $|\nabla\times\mathbf{u}|_{rms}$ are greater in 2D than in 3D. However, Fig. 10b shows that $|\nabla\times\mathbf{u}|_{rms}$ in 2D starts decreasing after 1 ns, which we will show is due to an upscale vortical energy transfer discussed in Section VI A. In contrast, $|\nabla\times\mathbf{u}|_{rms}$ in 3D increases over the entire duration of the simulation as seen from Fig. 10b. From the ratio $|\nabla\cdot\mathbf{u}|_{rms}/|\nabla\times\mathbf{u}|_{rms}$ (see Appendix Fig. 21b), which is a measure of compressibility levels at small scales, we can infer that the 2D jet also exhibits higher small-scale compressibility levels than its 3D counterpart at $t = 3.5$ ns.

III. ANALYZING MULTISCALE DYNAMICS AND ENERGY TRANSFER

A. Coarse Graining

The coarse-graining approach allows for analyzing the dynamics at different scales in a complex flow, which has proven to be a natural and versatile framework to understand scale interactions[40,54–57]. The approach is standard in partial differential equations and distribution theory[58,59]. It became common in large eddy simulation (LES) modeling[39] of turbulence thanks to the foundational works of Leonard[60] and Germano[61]. Ref.[62] provides an overview of coarse-graining and its connection to other methods in physics.

For any field $\mathbf{a}(\mathbf{x})$, a coarse-grained or (low-pass) filtered version of this field, which contains spatial variations at scales $> \ell$, is defined in n-dimensions as

$$\bar{\mathbf{a}}_\ell(\mathbf{x}) = \int \mathrm{d}^n\mathbf{r}\ G_\ell(\mathbf{r}-\mathbf{x})\,\mathbf{a}(\mathbf{r}), \tag{4}$$

Here, G_ℓ is a convolution kernel derived from the "father" kernel $G(\mathbf{s})$ (borrowing the term from wavelet analysis[63]). $G(\mathbf{s})$ is normalized, $\int \mathrm{d}^n\mathbf{s}\,G(\mathbf{s}) = 1$. It is an even function such that $\int \mathbf{s}\,G(\mathbf{s})\,\mathrm{d}^n\mathbf{s} = 0$, which ensures that local averaging is symmetric. $G(\mathbf{s})$ also has its main support (or variance) over a region of order unity in diameter, $\int \mathrm{d}^n\mathbf{s}\,|\mathbf{s}|^2\,G(\mathbf{s}) = O(1)$. The

dilated version of the kernel, $G_\ell(\mathbf{r}) = \ell^{-n} G(\mathbf{r}/\ell)$, is a function of dimensional position vector $\mathbf{r}$ and inherits all those properties, except that its main support is over a region of diameter ℓ.

An example is the Boxcar kernel in non-dimensional coordinates,

$$G(\mathbf{s}) = \begin{cases} 1, & \text{if } |s_i| < 1/2 \text{ for } i = 1,\ldots,n, \\ 0, & \text{otherwise,} \end{cases} \tag{5}$$

and its dilated version in dimensional coordinates,

$$G_\ell(\mathbf{r}) = \begin{cases} \ell^{-n}, & \text{if } |r_i| < \ell/2 \text{ for } i = 1,\ldots,n, \\ 0, & \text{otherwise.} \end{cases} \tag{6}$$

The scale decomposition in eq. (4) is essentially a partitioning of scales for a field into large scales ($\gtrsim \ell$), captured by $\overline{\mathbf{a}}_\ell$, and small scales ($\lesssim \ell$), captured by the residual $\mathbf{a}'_\ell = \mathbf{a} - \overline{\mathbf{a}}_\ell$. In the following analyses, we use the Boxcar kernel in eq. (6) for coarse-graining. With non-periodic boundary conditions, such as with our simulation domains here, filtering near the boundary requires a choice for the fields beyond the boundary. It was shown in previous works that a natural choice is to extend the domain beyond the physical boundaries with values compatible with the boundary conditions[64–66]. However, over the times we analyze the jets in this work, flow across the domain boundaries is negligible. With consideration to the Helmholtz decomposition we use in Section VI and the ease of its implementation, we mirror (or reflect) the variables across the boundary when coarse-graining. In the Appendix Figs. 22-24, we show that mirroring has negligible effect on the results compared to extending the variables beyond the domain boundaries using the true boundary conditions.

B. Mechanisms of Energy Transfer

Diagnosing the scale-dependent kinetic energy budget in constant-density turbulence typically focuses on analyzing kinetic energy based on the coarse velocity field, $\frac{1}{2}\rho_0|\overline{\mathbf{u}}_\ell|^2$ (e.g., Refs.[39,62]). However, in the presence of significant density variations, kinetic energy $\frac{1}{2}\rho|\mathbf{u}|^2$ is non-quadratic and its decomposition as a function of scale is not as straightforward[34]. Several different decompositions have been proposed in the literature, such as $\frac{1}{2}\overline{\rho}_\ell|\overline{\mathbf{u}}_\ell|^2$ (e.g., Refs.[67–70]) and $\frac{1}{2}|\overline{(\sqrt{\rho}\mathbf{u})}_\ell|^2$ (e.g., Refs.[37,71–73]). However, Zhao & Aluie[74] showed that these scale decompositions violate the "inviscid criterion", which requires that viscous effect be negligible at sufficiently large scales. They also demonstrated that the Favre decomposition[34,75], $\frac{1}{2}\overline{\rho}_\ell|\widetilde{\mathbf{u}}_\ell|^2$, satisfies the inviscid criterion, where the Favre filtered velocity is density-weighted according to

$$\widetilde{\mathbf{u}}_\ell = \overline{\rho\mathbf{u}}_\ell / \overline{\rho}_\ell. \tag{7}$$

The KE budget at scales larger than an arbitrary ℓ is derived from the compressible Navier-Stokes equations[34,76],

$$\partial_t \overline{\rho}_\ell \frac{|\widetilde{\mathbf{u}}_\ell|^2}{2} + \boldsymbol{\nabla}\cdot\mathbf{J}_\ell = -\Pi_\ell - \Lambda_\ell + \overline{P}_\ell \boldsymbol{\nabla}\cdot\overline{\mathbf{u}}_\ell - D_\ell + \varepsilon_\ell^{inj}. \tag{8}$$

Here, $\mathbf{J}_\ell(\mathbf{x})$ is spatial transport of large-scale kinetic energy, $-\overline{P}_\ell \boldsymbol{\nabla}\cdot\overline{\mathbf{u}}_\ell$ is large-scale pressure dilatation, $D_\ell(\mathbf{x})$ is viscous dissipation acting on scales larger than ℓ, and $\varepsilon_\ell^{inj}(\mathbf{x})$ is the energy injected due to external forcing. These terms are defined by Ref.[34] in eqs. 16–18. Deformation work, $\Pi_\ell(\mathbf{x})$, and baropycnal work, $\Lambda_\ell(\mathbf{x})$, account for the energy transfer across scales, and are defined as

$$\Pi_\ell(\mathbf{x}) = -\overline{\rho}\,\partial_j \widetilde{u}_i\, \widetilde{\tau}(u_i, u_j), \tag{9}$$

$$\Lambda_\ell(\mathbf{x}) = \frac{1}{\overline{\rho}}\,\partial_j \overline{P}\,\overline{\tau}(\rho, u_j), \tag{10}$$

where the 2^{nd}-order generalized central moment[61] is

$$\overline{\tau}(f,g) \equiv \overline{(fg)}_\ell - \overline{f}_\ell \overline{g}_\ell, \tag{11}$$

and its Favre density-weighted analogue[34,38] is

$$\widetilde{\tau}(f,g) \equiv \widetilde{(fg)}_\ell - \widetilde{f}_\ell \widetilde{g}_\ell. \tag{12}$$

Physically, $\widetilde{\tau}(u_i,u_j)$ in eq. (9) represents the subscale stress tensor (per unit mass) exerted by scales $< \ell$ on the larger scale flow, and $\overline{\tau}(\rho,u_j)$ in eq. (10) represents the subscale mass flux due to scales $< \ell$. As $\Pi_\ell(\mathbf{x})$ and $\Lambda_\ell(\mathbf{x})$ appear in eq. (8), they are defined to be positive energy transfer from large scales to small scales.

$\Pi_\ell(\mathbf{x})$ and $\Lambda_\ell(\mathbf{x})$ contain all information needed to quantify the exchange of energy between the two sets of scales, $> \ell$ and $< \ell$. Since we have complete knowledge of the dynamics at all scales resolved in a simulation, $\Pi_\ell(\mathbf{x})$ and $\Lambda_\ell(\mathbf{x})$ can be calculated exactly at every point $\mathbf{x}$ in the domain and at any instant in time t. It is often not possible from simulations or observations to resolve all scales present in the real system. Therefore, computing $\Pi_\ell(\mathbf{x})$ and $\Lambda_\ell(\mathbf{x})$ is only measuring the dynamical coupling between scales present in the data.

In many instances, standard tools that were developed and used in the turbulence literature to the study of cross-scale transfer are only strictly valid to analyze homogeneous isotropic incompressible flows. Consequently, calculations of the energy transfer rates in HED hydrodynamic applications that use these tools may give ambiguous results for inhomogeneous flows, such as the jet in Fig. 6. The problem arises because there are several possible definitions for the scale-transfer terms, $\Pi_\ell(\mathbf{x})$ and $\Lambda_\ell(\mathbf{x})$, as we now elaborate.

Definitions (9),(10) for the scale-transfer of energy in budget (8) are not unique with other definitions possible (see examples in Refs.[41,64]). The difference between any two of these definitions is a divergence term, $\boldsymbol{\nabla}\cdot(\ldots)$, which amounts to a reinterpretation of which terms in budget (8) represent transfer of energy across scales and which terms redistribute (or transport) energy in space, $\mathbf{J}_\ell(\mathbf{x})$. There is an infinite number of ways to reorganize terms in budget (8) and, thus, an infinite number of possible definitions for the transfer of kinetic energy between scales. This freedom in defining $\Pi_\ell(\mathbf{x})$ can be thought of as a *gauge freedom*[64].

In a homogeneous flow, spatial averages of all these definitions are equal because their difference is a divergence that is

TABLE III. Domain-averaged cumulative KE at $t = 3.5$ ns.

Cumulative Energy (erg/cm^3)	$k_\ell = 1$	KE^{tot}
KE_{2D}	4.09×10^{10}	6.89×10^{10}
KE_{3D}	3.61×10^{10}	6.86×10^{10}
$KE_{2D} - KE_{3D}$	$\mathbf{4.80 \times 10^9}$	2.96×10^8

zero, $\langle \boldsymbol{\nabla} \cdot (\ldots) \rangle = 0$. On the other hand, if one considers inhomogeneous flows, such as the jet in Fig. 6, or if one wishes to analyze the cascade locally in space without spatial averaging, then such definitions can differ qualitatively as well as quantitatively (see Ref.[64] for examples). Definitions (9),(10) are proper measures of the energy scale-transfer because they satisfy two important physical criteria: (i) Galilean invariance and (ii) vanish in the absence of subscale motion[77]. Using such criteria to choose the scale-transfer definitions may be thought of as *gauge fixing*. Regarding the second criterion, both scale-transfer terms vanish identically at every location $\mathbf{x}$ when ℓ is the grid scale or smaller[77]. The latter is a physically important constraint since scales smaller than ℓ should not influence the larger scale flow if those scales do not exist.

In the remainder of this paper, the subscript ℓ is omitted for the variables defined above if there is no risk of ambiguity. In what follows, we shall use k_ℓ to represent the "filtering wavenumber"[78] corresponding to length scale ℓ,

$$k_\ell \equiv L/\ell, \tag{13}$$

with $L = 0.25$ cm being the domain size along the x-direction, which we use here as a reference scale. Note that k_ℓ is not a Fourier wavenumber, just a proxy for scale from the coarse-graining decomposition.

IV. ENERGY TRANSFER IN THE ENTIRE DOMAIN

We have already shown in Fig. 5 that KE in 2D and 3D is almost identical at $t = 3.5$ ns, differing by only 0.47%. However, the distribution of this KE among length scales differs significantly between 2D and 3D.

A. Cumulative Energy

Coarse KE in eq. (8), $\rho_\ell |\widetilde{\mathbf{u}}_\ell|^2/2$, quantifies the cumulative KE at all scales larger than ℓ. Taking $k_\ell = L/\ell = 1$, Fig. 11 shows that KE in 2D at scales larger than $L = 0.25$ cm exceeds that in 3D. This difference of 4.80×10^9 erg/cm^3 in KE content at large scales is highlighted in Table III, which is greater by more than an order of magnitude compared to the 2.96×10^8 erg/cm^3 (0.47% difference) in total KE. This is consistent with the bulk jet flow in 2D being faster than in 3D (Fig. 6). Indeed, Fig. 25 in the Appendix shows that most of this difference between 2D and 3D is from the y-component of KE, $\rho_\ell |\widetilde{(u_y)}_\ell|^2/2$, due to the flow in the axial direction. Fig. 11 also shows that for larger $k_\ell = 2,4$ values, the difference between 2D and 3D diminishes. This is to be expected since increasing k_ℓ is equivalent to including smaller scales in coarse KE metric, which converges to the total KE, $\rho_\ell |\widetilde{\mathbf{u}}_\ell|^2/2 \to \rho |\mathbf{u}|^2/2$ in the limit $k_\ell \to \infty$ or, equivalently, $\ell \to 0$. We remind the reader that total KE is almost identical in 2D and 3D (Table III and Fig. 5).

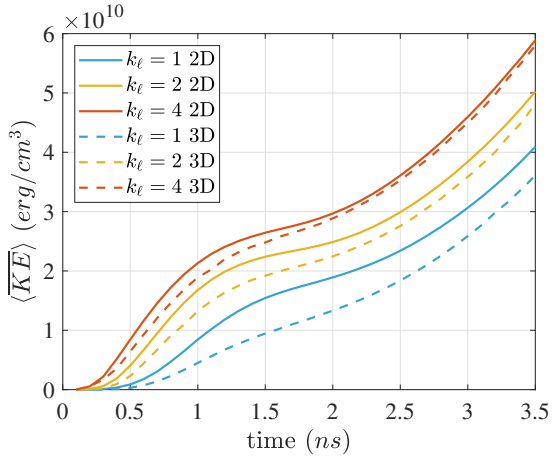

FIG. 11. Domain-averaged coarse KE, $\langle \overline{\rho}_\ell |\widetilde{\mathbf{u}}_\ell|^2/2 \rangle$, at all scales $> \ell$. Here, filtering wavenumber $k_\ell = L/\ell$ is not a Fourier wavenumber, just a proxy for scale ℓ from the coarse-graining decomposition. The largest scales (blue) in 2D have more KE than in 3D, even though total KE is almost identical in both 2D and 3D (Fig. 5). This can be seen here from having the 2D and 3D plots getting closer (solid and dashed) as we include smaller scales (larger k_ℓ, yellow and red) in the coarse KE.

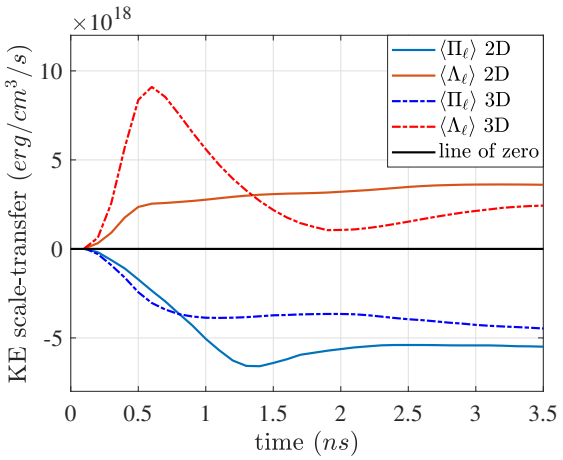

FIG. 12. Domain-averaged deformation work, $\langle \Pi_\ell \rangle$, and baropycnal work, $\langle \Lambda_\ell \rangle$, across scale $k_\ell = 1$. In both 2D and 3D, $\langle \Pi_\ell \rangle$ transfers energy upscale and $\langle \Lambda_\ell \rangle$ transfers energy downscale at all times.

B. Kinetic Energy Transfer at Selected Scale

To explain the aforementioned large scale ($\ell > L = 0.25$ cm) KE difference between 2D and 3D, we analyze the KE scale-transfer, Π_ℓ and Λ_ℓ in eqs. (9),(10). Fig. 12 show the time series of domain-averaged Π_ℓ and Λ_ℓ evaluated at

TABLE IV. Domain-averaged KE scal
1 integrated over the entire time durati

Energy transferred (erg/cm^3)	$\int \langle \Pi \rangle dt$
2D	-1.64×10
3D	-1.22×10
difference: 2D−3D	-4.11×10

$k_\ell = L/\ell = 1$. In both 2D and 3 domain-averaged, indicating a tra scales smaller than L to larger sca pansion and spread as the jet prop $\Lambda > 0$ in both 2D and 3D when dc downscale transfer. As discussed Refs.[32,34], energy by baropycnal v lease (or storage, if $\Lambda < 0$) of poter gradients acting against density va sure gradient arises near the ablatic

Table IV shows that the large tween 2D and 3D can be attributed scale-transfer. Π_ℓ and Λ_ℓ represent energy transfer rates (in erg/s/cm^3). Integrating Π_ℓ and Λ_ℓ over the duration of the simulation from $t = 0$ to 3.5 ns, we see in Table IV that there is 4.60×10^9 erg/cm^3 excess energy received by the large scales ($\ell > L = 0.25$ cm) in 2D compared to 3D. This value matches the large scale KE difference of 4.80×10^9 erg/cm^3 between 2D and 3D in Table III remarkably well[79], to within 4%. Since Π and Λ are the only terms that transfer KE across scales using our coarse-graining decomposition (eq. (8)), we can infer that differences between 2D and 3D in the jet's bulk speed and distance travelled (Fig. 6) are due to differences in KE scale-transfer. In the rest of this paper, we explore a physical origin for these differences in KE scale-transfer between 2D and 3D.

V. SUBSCALE STRESS AND THE TURBULENT REGION

From Fig. 6, there are notable differences between the 2D and 3D jets near the leading edge, where the flow is suggestive of turbulence. To objectively quantify the turbulence intensity, it is traditional to apply a Reynolds decomposition[23], $u_i = \langle u_i \rangle + u_i'$, to separate the velocity field into a mean part $\langle u_i \rangle$ and a fluctuating component u_i', where $\langle ... \rangle$ is an ensemble average. The Reynolds stress tensor, $\langle u_i' u_j' \rangle$, is typically used to quantify the turbulent fluctuations[22,23,80].

However, there are a few disadvantages of such an approach that make it undesirable for our purposes. For one, it requires an ensemble average, which is computationally costly and in practice is often taken to be a temporal average if the flow is in a statistically steady state, which our jets are not, or a spatial average along a statistically homogeneous direction. While the 3D jet is statistically homogeneous in the azimuthal direction at any time, the 2D jet lacks any fluctuations along that direction by definition, making a comparison between 2D and 3D using a Reynolds decomposition unjustifiable. Another disadvantage of a Reynolds decomposition is its inability to inform us about the scales at which such turbulence exists[81,82]. It is possible to use the analogue of the Reynolds stress $\langle u_i' u_j' \rangle$ within the coarse-graining approach, which is the subscale stress (per unit mass) as shown by Germano[61],

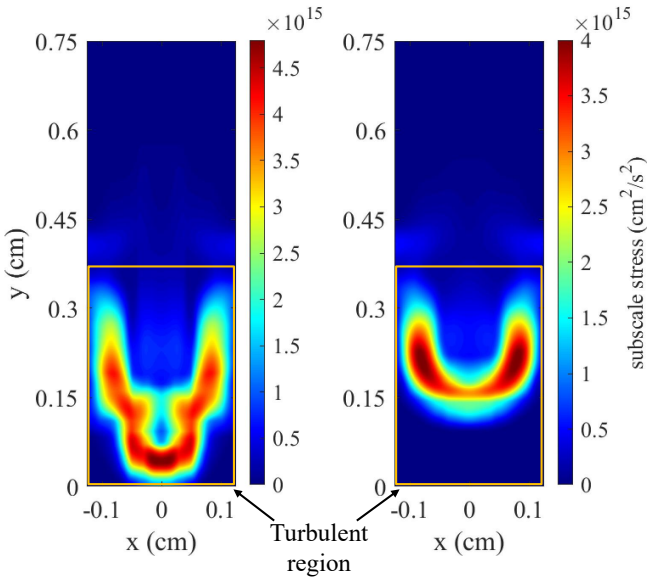

FIG. 13. Magnitude of (left) 2D and (right) 3D subscale stress, $|\overline{\tau}_\ell(u_i,u_j)| = |\overline{(u_i u_j)}_\ell - \overline{(u_i)}_\ell \overline{(u_j)}_\ell|$, at $k_\ell = 2$. Sub-domain outlined by a box is used to study the energy scale-transfer in the "turbulent" region.

$$\overline{\tau}_\ell(u_i,u_j) = \overline{(u_i u_j)}_\ell - \overline{(u_i)}_\ell \overline{(u_j)}_\ell. \tag{14}$$

The subscale stress is a rank-2 tensor, where each tensor component is a 2^{nd}-order generalized central moment[61] defined in eq. (11). The subscale stress quantifies the momentum flux contribution from subscales[39,41], *i.e.*, scales smaller than ℓ. Taking the length scale $\ell = L/2$ (*i.e.*, $k_\ell = 2$), the subscale stress magnitude at 3.5 ns is shown in Fig. 13. Since the dominant velocity component is in the y-direction, the magnitude of $\overline{\tau}_\ell(u_i,u_j)$ in both 2D and 3D is predominantly from by the tensor component $\overline{\tau}_\ell(u_y,u_y)$. Comparing 2D and 3D in Fig. 13, we see that the high-intensity subscale stress occurs at the front of the jets but with a marked difference at the leading edge along the jet axis. The 2D jet has pronounced stress at the leading edge between approximately $x = -0.05$ cm and 0.05 cm, which is absent in the 3D jet. The structures giving rise to this stress will be discussed below in Section VI B. The stress morphology in Fig. 13 justifies a focus on the lower half of the domain (y < 0.375 cm, highlighted boxes in Fig. 13) in an attempt to glean insight into differences in the KE scale-transfer between 2D and 3D.

VI. HELMHOLTZ DECOMPOSITION

Applying the Helmholtz decomposition to the velocity, $\mathbf{u} = \mathbf{u}^d + \mathbf{u}^s$, partitions it into a dilatational component, $\mathbf{u}^d$, and a solenoidal component, $\mathbf{u}^s$. Their curl-free ($\boldsymbol{\nabla} \times \mathbf{u}^d = 0$) and

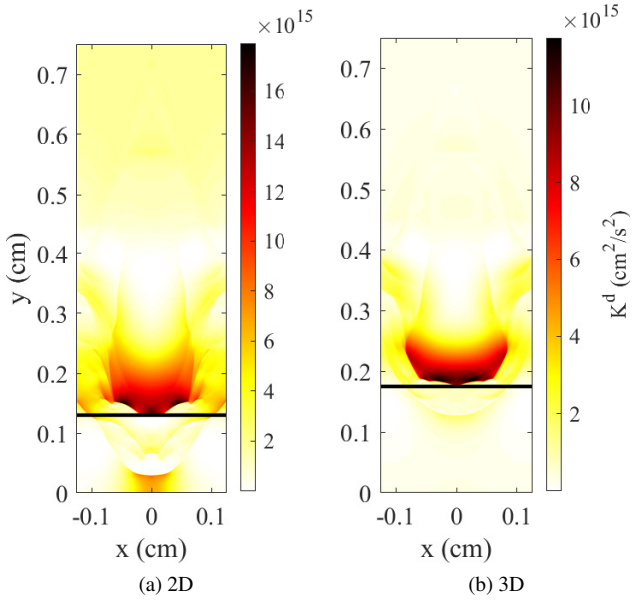

FIG. 14. Dilatational kinetic energy, $K^d = u_i^d u_i^d$. High-intensity K^d represents structures near the shock and have a similar shape between 2D and 3D. The shock front is marked by a horizontal black line.

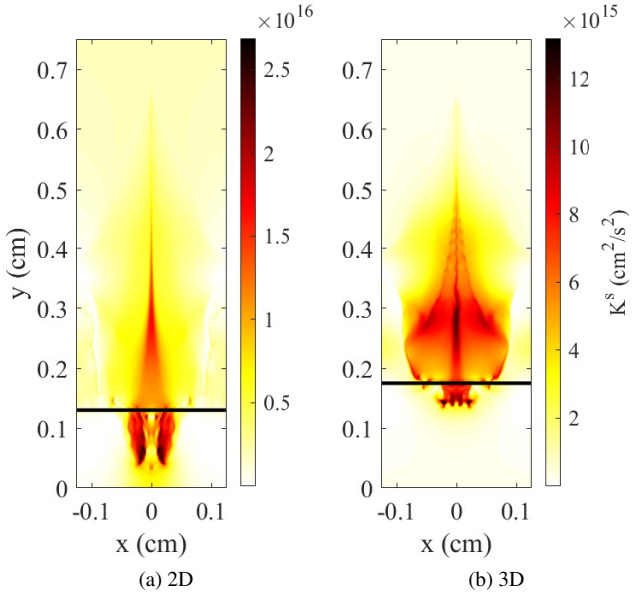

FIG. 15. Solenoidal kinetic energy, $K^s = u_i^s u_i^s$. High-intensity K^s mainly appear at leading edge of the jet and displays marked differences between 2D and 3D. Horizontal black lines are the same as in Fig. 14 and indicate the position of shock fronts.

divergence-free ($\nabla \cdot \mathbf{u}^s = 0$) properties[83] allow us to explore the dominant flow components, such as shocks and vorticity, that may contribute to the jet traveling farther in 2D than in 3D. To perform the Helmholtz decomposition, the domain is mirrored to create periodic boundary conditions. While our choice for dealing with the boundary conditions by mirroring is not unique, we shall see that our results are physically meaningful. Dilatational and solenoidal specific kinetic energy (*i.e.* per unit mass), $K^d = u_i^d u_i^d$ and $K^s = u_i^s u_i^s$, respectively, are shown in Figs. 14,15.

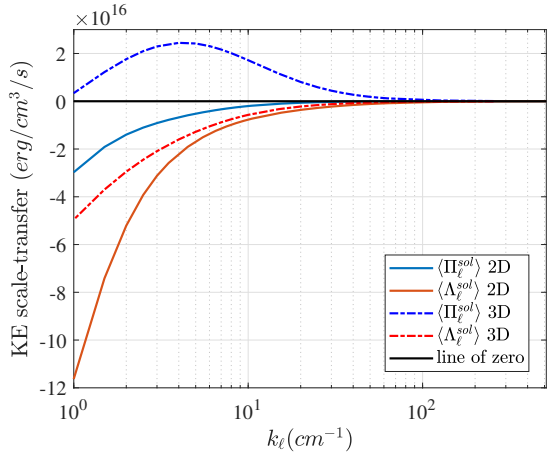

FIG. 16. Deformation work, $\langle \Pi_\ell^{sol} \rangle$, and baropycnal work, $\langle \Lambda_\ell^{sol} \rangle$, due to the solenoidal flow and averaged over the subdomain ($y <$ 0.375 cm) highlighted in Fig. 13, plotted here as a function of filtering wavenumber k_ℓ at $t = 3.5$ ns. The sign difference in $\langle \Pi_\ell^{sol} \rangle$ shows the qualitative contrast of the dynamics between the 2D and 3D jets. In 3D, deformation work from the vortical flow transfers KE downscale, $\langle \Pi_\ell^{sol} \rangle > 0$, whereas it transfers KE upscale in 2D, which sustains large-scale coherent vortical structures near the leading edge of the 2D jet as seen in Figs. 17-19.

For both the 2D and 3D jets, we can see from K^d in Fig. 14 that there is a marked discontinuity (underscored by a horizontal black line in Fig. 14) at the same y-location where the velocity is discontinuous in Fig. 6. To leading order, the structure of K^d in Fig. 14 is similar between 2D and 3D aside from a difference in their y-location.

Relative to K^d, the solenoidal flow K^s in Fig. 15 shows obvious differences between 2D and 3D. The highest intensity solenoidal flow in 2D is more collimated along the jet axis compared to that in 3D. There is also significant post-shock ($y \approx 0$ to 0.13 cm) solenoidal flow activity near the leading edge of the 2D jet, which suggests the presence of vorticity that is absent near the leading edge of the 3D jet. This suggests that differences in the KE scale-transfer are significantly influenced by the solenoidal component in the turbulent region near the leading edge, which we shall now analyze.

A. Deformation and Baropycnal Work

Using the Helmholtz decomposition, we can investigate the contribution of the solenoidal and dilatational flow to Π and Λ, which we denote by Π^{sol}, Π^{dil}, Λ^{sol} and Λ^{dil}. These are obtained by replacing $\mathbf{u}$ with $\mathbf{u}^s$ or $\mathbf{u}^d$ in eq. (9) and (10), respectively. Note that $\Pi^{sol} + \Pi^{dil} \neq \Pi$ since the decomposition also yields transfer terms involving both $\mathbf{u}^s$ and $\mathbf{u}^d$, which we do not analyze here and focus instead on the pure solenoidal behavior.

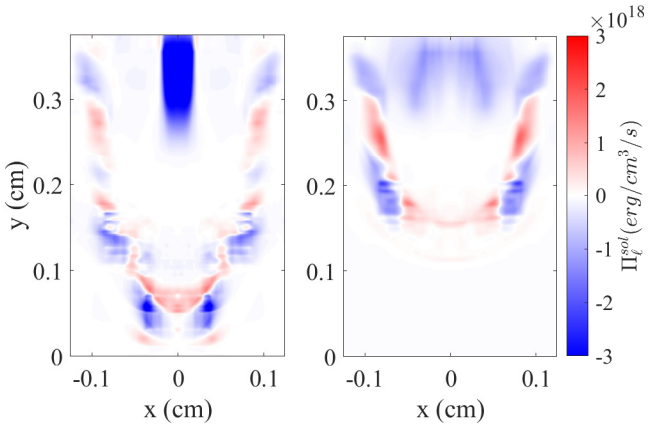

(a) 2D (b) 3D

FIG. 17. Visualization of solenoidal deformation work, Π^{sol}_ℓ, in the turbulent domain ($y < 0.375$ cm) at $k_\ell = 2$. Marked differences can be seen at the leading edge where Π^{sol}_ℓ has negative values in 2D panel (a) at $y \approx 0.05$ cm, which are absent in 3D panel (b).

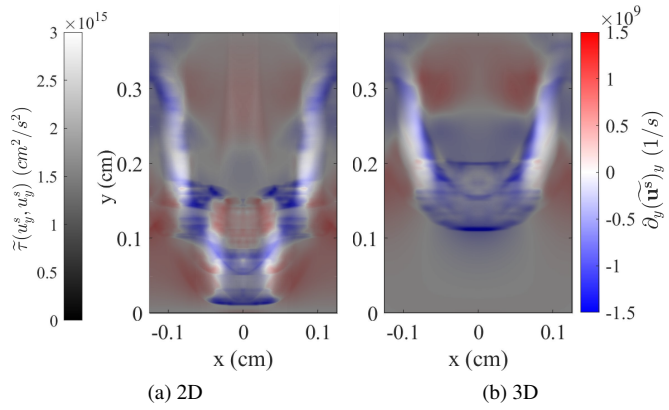

(a) 2D (b) 3D

FIG. 18. Correlating coarse velocity gradients, $\partial_y(\widetilde{\mathbf{u}}^s)_y$ (red-blue colormap), with subscale stress, $\widetilde{\tau}(u^s_y, u^s_y)$ (gray-scale map), at scale $k_\ell = 2$. Since subscale stress is positive semi-definite, the gray-scale map highlights regions of strong scale-transfer. The main differences are seen at the flanks of the 2D jet's leading edge, $|x| = 0.03$ to 0.05 cm and $y < 0.1$ cm, where $\partial_y(\widetilde{u}^s)_y$ is mostly positive, implying an upscale transfer in 2D as seen in Fig. 17 that is absent in 3D.

The opposing signs of Π^{sol} between 2D and 3D in Fig. 16 shows the qualitative contrast of the dynamics. In 3D, deformation work from the vortical flow transfers KE downscale, $\langle \Pi^{sol}_\ell \rangle > 0$, whereas it transfers KE upscale in 2D, which sustains large-scale coherent vortical structures near the leading edge of the 2D jet as we shall see below in Figs. 17-19.

The upscale transfer of KE in 2D by Π^{sol} in Fig. 16 is similar to the upscale cascade seen in 2D variable density Rayleigh-Taylor turbulence[32]. It is also similar to 2D constant-density turbulence[30,84,85] due to the absence of vortex stretching and strain self-amplification[28]. Even though the the magnitudes of Π^{sol} and Λ^{sol} in Fig. 16 are smaller than total Π and Λ over the entire domain in Fig. 12, the vorticity dynamics at the leading edge can have a disproportionate effect on the jet's traveling distance and bulk flow evolution as we shall discuss below.

B. Circulation Mechanism

To understand the mechanistic cause of differences in Π^{sol} between 2D and 3D, we probe its tensorial components. Fig. 17 visualizes Π^{sol}_ℓ at $k_\ell = 2$. We can see obvious differences between 2D and 3D in the sign of Π^{sol}_ℓ at the leading edge of the jet, which seem to correlate with differences seen in Fig. 15. As defined in eq. (9), Π^{sol} is a contraction between the velocity gradient tensor, $-\partial_j(\widetilde{u}^s)_i$, and the subscale stress tensor, $\overline{\rho}\widetilde{\tau}(u^s_i, u^s_j)$. To understand the sign of Π^{sol}, we focus on the tensor components $i, j = 2$ (y-components), which make the dominant contribution to the spatially averaged Π^{sol}.

The subscale stress component $\overline{\rho}\widetilde{\tau}(u^s_y, u^s_y)$ is mathematically guaranteed to be positive semi-definite at every point in the domain[34,78,86]. This is shown in Fig. 18. Therefore, the sign of Π^{sol}_ℓ from the y-components is the same as that of $-\partial_y(\widetilde{u}^s)_y$. Fig. 18 visualizes $\partial_y(\widetilde{u}^s)_y$ with red/blue indicating positive/negative values, implying upscale/downscale KE transfer (Π^{sol}_ℓ from $i, j = 2$ components is negative/positive). Overlapping the colormap in Fig. 18 is a gray-scale map of $\widetilde{\tau}(u^s_y, u^s_y)$, which, being positive semi-definite, highlights regions of strong sub-scale stress and, therefore, strong scale-transfer.

Both panels of Fig. 18 at $y > 0.15$ cm are roughly similar to leading order in regions of strong stress. In those highlighted regions at the jet flanks at $y > 0.15$ cm, we see that $\partial_y(\widetilde{u}^s)_y$ is mostly negative, implying downscale transfer in both 2D and 3D. The main differences are seen at the flanks of the 2D jet's leading edge, $|x| = 0.03$ to 0.05 cm and $y < 0.1$ cm, where $\partial_y(\widetilde{u}^s)_y$ is mostly positive, implying an upscale transfer in 2D that is absent in 3D.

At the flanks of the leading edge ($|x| = 0.03$ to 0.05 cm) in 2D, we see in Fig. 18 that $\partial_y(\widetilde{\mathbf{u}}^s)_y$ switches sign along the y-direction between $y \approx 0.05$ cm and 0.1 cm. This is suggestive of vortical motion. Fig. 19 visualizes the flow streamlines superposed over $\partial_y(\widetilde{\mathbf{u}}^s)_y$. From the streamlines in Fig. 19, we can see clearly two coherent vortical structures at the leading edge of the 2D jet, which are absent from the 3D jet. The streamlines in Fig. 19 are consistent with observations we made above that the flow at $y > 0.15$ cm is roughly similar between 2D and 3D (see also Fig. 29 in Appendix). The main difference is at $y < 0.15$ cm, where the coherent roll-up structure in the 2D jet at $y \approx 0.05$ cm is co-located with the upscale energy transfer seen at that same location in Fig. 17. This is indicative of the coherent roll-up being energized by the smaller scale turbulence created post-shock. Such an upscale scale-transfer is absent in 3D, which cannot sustain the coherent roll-up. Vorticity within this roll-up creates an effective velocity drift[86] that helps propel the 2D jet farther and keep it collimated relative to its 3D counterpart.

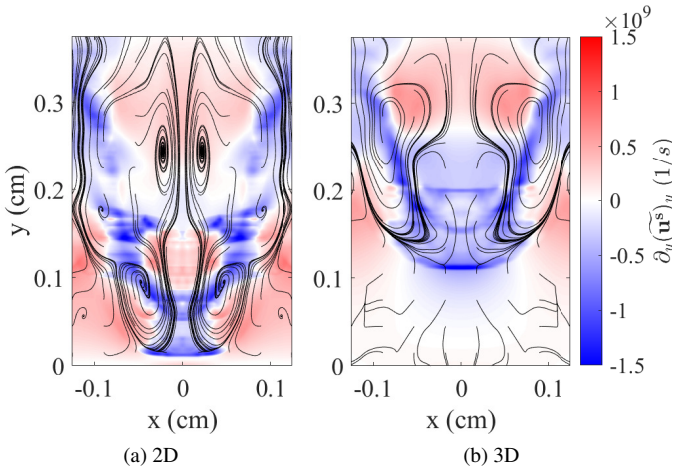

(a) 2D (b) 3D

FIG. 19. Correlating coarse velocity gradients, $\partial_y(\widetilde{\mathbf{u}^s})_y$ (red-blue colormap), with streamlines (black) superposed. The coherent vortical roll-up structure at the leading edge of the 2D jet is absent from the 3D jet. The roll-up in the 2D jet at $y \approx 0.05$ cm is co-located with the upscale energy transfer seen at that same location in Fig. 17, indicating that the roll-up in 2D is energized by the smaller scale turbulence.

VII. CONCLUDING REMARKS

In this paper, we demonstrated a methodology for diagnosing the multiscale dynamics and energy transfer in complex HED flows with realistic driving and boundary conditions. While it is well known that 2D modeling underestimates the proneness of the flow to instabilities, what we have shown here is that 2D modeling also suffers from significant spurious energization of the bulk flow by instabilities. The energization of the roll-up structures via an upscale transfer from smaller scale turbulence in Figs. 17-19 brings to the fore some of the hydrodynamics artefacts associated with 2D modeling, reinforcing recent findings[32].

In HED applications such as ICF, 2D simulations remain to be the main "work horse" for experimental design[17–19] as routine 3D simulations are prohibitively expensive[3]. Our hope from this work is to highlight the trade-off between 2D and 3D flow physics, which may not be as widely appreciated as trade-offs from approximating other system components such as the laser drive or the hohlraum. While computational realities may prevent the community from routinely conducting 3D hydrodynamic modeling in the foreseeable future, we hope that this work (see also Ref.[32]) highlights the need to alleviate some of the hydrodynamic artefacts associated with 2D models.

By demonstrating the applicability of coarse-graining for comparing the multiscale dynamics and energy transfer between 2D and 3D, we have shown that this methodology can help with inter-model comparison and validation. We believe that future attempts at alleviating some of the 2D hydrodynamic artefacts would have to use this approach, at least in some fashion, for testing and model development. After all, the approach has plenty in common with Large Eddy Simulation modeling, which is a well-established field in fluid dynamics[39].

ACKNOWLEDGMENTS

This work was supported by CMAP, an NSF Physics Frontiers Center, under grant PHY-2020249. Partial support from grants DE-SC0020229, DE-SC0019329, and CBET-2143702 is also acknowledged. HA was also supported by US DOE grants DE-SC0014318, DE-SC0019329, US NSF grants OCE-2123496, PHY-2206380, US NASA grant 80NSSC18K0772, and US NNSA grants DE-NA0003856, DE-NA0003914, DE-NA0004134. JS was supported by DE-SC0019329, DE-NA0003914, and DE-NA0004134. Computing time was provided by NERSC under Contract No. DE-AC02-05CH11231.

AUTHOR DECLARATIONS

Conflict of Interest

The authors have no conflicts to disclose.

DATA AVAILABILITY

The data that supports the findings of this study are available from the corresponding authors upon reasonable request.

REFERENCES

[1] B. E. Blue, S. V. Weber, S. G. Glendinning, N. E. Lanier, D. T. Woods, M. J. Bono, S. N. Dixit, C. A. Haynam, J. P. Holder, D. H. Kalantar, B. J. MacGowan, A. J. Nikitin, V. V. Rekow, B. M. Van Wonterghem, E. I. Moses, P. E. Stry, B. H. Wilde, W. W. Hsing, and H. F. Robey, "Experimental investigation of high-Mach-number 3d hydrodynamic jets at the National Ignition Facility," Phys. Rev. Lett. **94**, 095005 (2005).

[2] A. M. Khokhlov, P. A. Höflich, E. S. Oran, J. C. Wheeler, L. Wang, and A. Y. Chtchelkanova, "Jet-induced explosions of core collapse supernovae," The Astrophysical Journal **524**, L107 (1999).

[3] D. S. Clark, C. R. Weber, J. L. Milovich, J. D. Salmonson, A. L. Kritcher, S. W. Haan, B. A. Hammel, D. E. Hinkel, O. A. Hurricane, O. S. Jones, M. M. Marinak, P. K. Patel, H. F. Robey, S. M. Sepke, and M. J. Edwards, "Three-dimensional simulations of low foot and high foot implosion experiments on the National Ignition Facility," Physics of Plasmas **23**, 056302 (2016).

[4] A. Zylstra, D. Casey, A. Kritcher, L. Pickworth, B. Bachmann, K. Baker, J. Biener, T. Braun, D. Clark, V. Geppert-Kleinrath, *et al.*, "Hot-spot mix in large-scale hdc implosions at nif," Physics of Plasmas **27**, 092709 (2020).

[5] B. M. Haines, J. P. Sauppe, B. J. Albright, W. S. Daughton, S. M. Finnegan, J. L. Kline, and J. M. Smidt, "A mechanism for reduced compression in indirectly driven layered capsule implosions," Physics of Plasmas **29**, 042704 (2022).

[6] S. R. Goldman, S. E. Caldwell, M. D. Wilke, D. C. Wilson, C. W. Barnes, W. W. Hsing, N. D. Delamater, G. T. Schappert, J. W. Grove, E. L. Lindman, J. M. Wallace, R. P. Weaver, A. M. Dunne, M. J. Edwards, P. Graham, and B. R. Thomas, "Shock structuring due to fabrication joints in targets," Physics of Plasmas **6**, 3327–3336 (1999), https://doi.org/10.1063/1.873572.

[7] S. R. Goldman, C. W. Barnes, S. E. Caldwell, D. C. Wilson, S. H. Batha, J. W. Grove, M. L. Gittings, W. W. Hsing, R. J. Kares, K. A. Klare, G. A. Kyrala, R. W. Margevicius, R. P. Weaver, M. D. Wilke, A. M. Dunne, M. J. Edwards, P. Graham, and B. R. Thomas, "Production of enhanced pressure regions due to inhomogeneities in inertial confinement fusion targets," Physics of Plasmas **7**, 2007–2013 (2000), https://doi.org/10.1063/1.874022.

[8] Y. Zhou, "Rayleigh–taylor and richtmyer–meshkov instability induced flow, turbulence, and mixing. i," Physics Reports **720**, 1–136 (2017).

[9] Y. Zhou, "Rayleigh–taylor and richtmyer–meshkov instability induced flow, turbulence, and mixing. ii," Physics Reports **723**, 1–160 (2017).

[10] T. Foglizzo, R. Kazeroni, J. Guilet, F. Masset, M. González, B. K. Krueger, J. Novak, M. Oertel, J. Margueron, J. Faure, *et al.*, "The explosion mechanism of core-collapse supernovae: Progress in supernova theory and experiments," Publications of the Astronomical Society of Australia **32**, e009 (2015).

[11] H.-T. Janka, T. Melson, and A. Summa, "Physics of core-collapse supernovae in three dimensions: A sneak preview," Annual Review of Nuclear and Particle Science **66**, 341–375 (2016), https://doi.org/10.1146/annurev-nucl-102115-044747.

[12] D. Radice, E. Abdikamalov, C. D. Ott, P. Mösta, S. M. Couch, and L. F. Roberts, "Turbulence in core-collapse supernovae," Journal of Physics G: Nuclear and Particle Physics **45**, 053003 (2018).

[13] F. Hanke, B. Müller, A. Wongwathanarat, A. Marek, and H.-T. Janka, "SASI ACTIVITY IN THREE-DIMENSIONAL NEUTRINO-HYDRODYNAMICS SIMULATIONS OF SUPERNOVA CORES," The Astrophysical Journal **770**, 66 (2013).

[14] I. Tamborra, F. Hanke, H.-T. Janka, B. Müller, G. G. Raffelt, and A. Marek, "SELF-SUSTAINED ASYMMETRY OF LEPTON-NUMBER EMISSION: A NEW PHENOMENON DURING THE SUPERNOVA SHOCK-ACCRETION PHASE IN THREE DIMENSIONS," The Astrophysical Journal **792**, 96 (2014).

[15] S. M. Couch and C. D. Ott, "THE ROLE OF TURBULENCE IN NEUTRINO-DRIVEN CORE-COLLAPSE SUPERNOVA EXPLOSIONS," The Astrophysical Journal **799**, 5 (2015).

[16] R. Betti and O. A. Hurricane, "Inertial-confinement fusion with lasers," Nature Physics **12**, 435–448 (2016).

[17] D. J. Schlossberg, G. P. Grim, D. T. Casey, A. S. Moore, R. Nora, B. Bachmann, L. R. Benedetti, R. M. Bionta, M. J. Eckart, J. E. Field, *et al.*, "Observation of hydrodynamic flows in imploding fusion plasmas on the national ignition facility," Phys. Rev. Lett. **127**, 125001 (2021).

[18] A. L. Kritcher, C. V. Young, H. F. Robey, C. R. Weber, A. B. Zylstra, O. A. Hurricane, D. A. Callahan, J. E. Ralph, J. S. Ross, K. L. Baker, *et al.*, "Design of inertial fusion implosions reaching the burning plasma regime," Nature Physics **18**, 251–258 (2022).

[19] A. L. Kritcher, A. B. Zylstra, D. A. Callahan, O. A. Hurricane, C. R. Weber, D. S. Clark, C. V. Young, J. E. Ralph, D. T. Casey, A. Pak, *et al.*, "Design of an inertial fusion experiment exceeding the lawson criterion for ignition," Phys. Rev. E **106**, 025201 (2022).

[20] B. M. Haines, R. C. Shah, J. M. Smidt, B. J. Albright, T. Cardenas, M. R. Douglas, C. Forrest, V. Y. Glebov, M. A. Gunderson, C. E. Hamilton, K. C. Henderson, Y. Kim, M. N. Lee, T. J. Murphy, J. A. Oertel, R. E. Olson, B. M. Patterson, R. B. Randolph, and D. W. Schmidt, "Observation of persistent species temperature separation in inertial confinement fusion mixtures," Nature Communications **11**, 544 (2020).

[21] M. Gatu Johnson, B. Haines, P. Adrian, C. Forrest, J. Frenje, V. Glebov, W. Grimble, R. Janezic, J. Knauer, B. Lahmann, F. Marshall, T. Michel, F. Séguin, C. Stoeckl, and R. Petrasso, "3d xrage simulation of inertial confinement fusion implosion with imposed mode 2 laser drive asymmetry," High Energy Density Physics **36**, 100825 (2020).

[22] H. Tennekes and J. L. Lumley, *A First Course in Turbulence* (The MIT Press, Cambridge, Massachusetts, 1972).

[23] S. B. Pope, *Turbulent flows* (Cambridge University Press, New York, 2000).

[24] V. BORUE and S. A. ORSZAG, "Local energy flux and subgrid-scale statistics in three-dimensional turbulence," Journal of Fluid Mechanics **366**, 1–31 (1998).

[25] G. L. Eyink, "Cascade of circulations in fluid turbulence," Phys. Rev. E **74**, 066302 (2006).

[26] G. L. Eyink, "Dissipative anomalies in singular euler flows," Physica D: Nonlinear Phenomena **237**, 1956–1968 (2008), euler Equations: 250 Years On.

[27] H. Xu, A. Pumir, and E. Bodenschatz, "The pirouette effect in turbulent flows," Nature Physics **7**, 709–712 (2011).

[28] P. L. Johnson, "Energy transfer from large to small scales in turbulence by multiscale nonlinear strain and vorticity interactions," Phys. Rev. Lett. **124**, 104501 (2020).

[29] R. H. Kraichnan, "Inertial Ranges in Two-Dimensional Turbulence," Physics of Fluids (1958-1988) **10**, 1417–1423 (1967).

[30] Z. XIAO, M. WAN, S. CHEN, and G. L. EYINK, "Physical mechanism of the inverse energy cascade of two-dimensional turbulence: a numerical investigation," Journal of Fluid Mechanics **619**, 1–44 (2009).

[31] G. Boffetta and R. E. Ecke, "Two-dimensional turbulence," Annual Review of Fluid Mechanics **44**, 427–451 (2012).

[32] D. Zhao, R. Betti, and H. Aluie, "Scale interactions and anisotropy in rayleigh–taylor turbulence," Journal of Fluid Mechanics **930**, A29 (2022).

[33] H. Aluie, "Compressible turbulence: The cascade and its locality," Phys. Rev. Lett. **106**, 174502 (2011).

[34] H. Aluie, "Scale decomposition in compressible turbulence," Physica D: Nonlinear Phenomena **247**, 54–65 (2013).

[35] H. Aluie, S. Li, and H. Li, "CONSERVATIVE CASCADE OF KINETIC ENERGY IN COMPRESSIBLE TURBULENCE," The Astrophysical Journal **751**, L29 (2012).

[36] A. G. Kritsuk, R. Wagner, and M. L. Norman, "Energy cascade and scaling in supersonic isothermal turbulence," Journal of Fluid Mechanics **729**, R1 (2013).

[37] J. Wang, Y. Yang, Y. Shi, Z. Xiao, X. T. He, and S. Chen, "Cascade of kinetic energy in three-dimensional compressible turbulence," Phys. Rev. Lett. **110**, 214505 (2013).

[38] G. L. Eyink and T. D. Drivas, "Cascades and dissipative anomalies in compressible fluid turbulence," Phys. Rev. X **8**, 011022 (2018).

[39] C. Meneveau and J. Katz, "Scale-Invariance and Turbulence Models for Large-Eddy Simulation," Ann. Rev. Fluid Mech. **32**, 1–32 (2000).

[40] G. L. Eyink, "Locality of turbulent cascades," Physica D: Nonlinear Phenomena **207**, 91–116 (2005).

[41] G. L. Eyink and H. Aluie, "Localness of energy cascade in hydrodynamic turbulence. i. smooth coarse graining," Physics of Fluids **21**, 115107 (2009), https://doi.org/10.1063/1.3266883.

[42] A. Lees and H. Aluie, "Baropycnal work: A mechanism for energy transfer across scales," Fluids **4** (2019), 10.3390/fluids4020092.

[43] A. S. Liao, S. Li, H. Li, K. Flippo, D. Barnak, K. V. Kelso, C. Fiedler Kawaguchi, A. Rasmus, S. Klein, J. Levesque, C. Kuranz, and C. Li, "Design of a new turbulent dynamo experiment on the omega-ep," Physics of Plasmas **26**, 032306 (2019), https://doi.org/10.1063/1.5081062.

[44] L. Waxer, D. Maywar, J. Kelly, T. Kessler, B. Kruschwitz, S. Loucks, R. McCrory, D. Meyerhofer, S. Morse, C. Stoeckl, and J. Zuegel, "High-energy petawatt capability for the omega laser," Opt. Photon. News **16**, 30–36 (2005).

[45] D. N. Maywar, J. H. Kelly, L. J. Waxer, S. F. B. Morse, I. A. Begishev, J. Bromage, C. Dorrer, J. L. Edwards, L. Folnsbee, M. J. Guardalben, S. D. Jacobs, R. Jungquist, T. J. Kessler, R. W. Kidder, B. E. Kruschwitz, S. J. Loucks, J. R. Marciante, R. L. McCrory, D. D. Meyerhofer, A. V. Okishev, J. B. Oliver, G. Pien, J. Qiao, J. Puth, A. L. Rigatti, A. W. Schmid, M. J. Shoup, C. Stoeckl, K. A. Thorp, and J. D. Zuegel, "OMEGA EP high-energy petawatt laser: progress and prospects," Journal of Physics: Conference Series **112**, 032007 (2008).

[46] B. Fryxell, K. Olson, P. Ricker, F. X. Timmes, M. Zingale, D. Q. Lamb, P. MacNeice, R. Rosner, J. W. Truran, and H. Tufo, "FLASH: An adaptive mesh hydrodynamics code for modeling astrophysical thermonuclear flashes," The Astrophysical Journal Supplement Series **131**, 273–334 (2000).

[47] P. Tzeferacos, A. Rigby, A. F. A. Bott, A. R. Bell, R. Bingham, A. Casner, F. Cattaneo, E. M. Churazov, J. Emig, F. Fiuza, C. B. Forest, J. Foster, C. Graziani, J. Katz, M. Koenig, C. K. Li, J. Meinecke, R. Petrasso, H. S. Park, B. A. Remington, J. S. Ross, D. Ryu, D. Ryutov, T. G. White, B. Reville, F. Miniati, A. A. Schekochihin, D. Q. Lamb, D. H. Froula, and G. Gregori, "Laboratory evidence of dynamo amplification of magnetic fields in a turbulent plasma," Nature Communications **9**, 591 (2018).

[48] P. Tzeferacos, M. Fatenejad, N. Flocke, C. Graziani, G. Gregori, D. Q. Lamb, D. Lee, J. Meinecke, A. Scopatz, and K. Weide, "Flash mhd simulations of experiments that study shock-generated magnetic fields," High Energy Density Physics **17, Part A**, 24 – 31 (2015).

[49]P. Tzeferacos, A. Rigby, A. Bott, A. R. Bell, R. Bingham, A. Casner, F. Cattaneo, E. M. Churazov, J. Emig, N. Flocke, F. Fiuza, C. B. Forest, J. Foster, C. Graziani, J. Katz, M. Koenig, C. K. Li, J. Meinecke, R. Petrasso, H. S. Park, B. A. Remington, J. S. Ross, D. Ryu, D. Ryutov, K. Weide, T. G. White, B. Reville, F. Miniati, A. A. Schekochihin, D. H. Froula, G. Gregori, and D. Q. Lamb, "Numerical modeling of laser-driven experiments aiming to demonstrate magnetic field amplification via turbulent dynamo," *Physics of Plasmas*, Physics of Plasmas **24**, 041404 (2017).

[50]"Flash user's guide," FLASH Center for Computational Science (2019).

[51]J. Macfarlane, "Ionmix - a code for computing the equation of state and radiative properties of lte and non-lte plasmas," Computer Physics Communications **56**, 259–278 (1989).

[52]P. MacNeice, K. M. Olson, C. Mobarry, R. de Fainchtein, and C. Packer, "PARAMESH: A parallel adaptive mesh refinement community toolkit," Computer Physics Communications **126**, 330–354 (2000).

[53]J. M. Foster, B. H. Wilde, P. A. Rosen, T. S. Perry, M. Fell, M. J. Edwards, B. F. Lasinski, R. E. Turner, and M. L. Gittings, "Supersonic jet and shock interactions," Physics of Plasmas **9**, 2251–2263 (2002), https://doi.org/10.1063/1.1468858.

[54]C. Meneveau, "Statistics of Turbulence Subgrid-Scale Stresses - Necessary Conditions and Experimental Tests," Physics of Fluids **6**, 815–833 (1994).

[55]G. L. Eyink, "Local energy flux and the refined similarity hypothesis," J. Stat. Phys. **78**, 335–351 (1995).

[56]M. Buzzicotti, M. Linkmann, H. Aluie, L. Biferale, J. Brasseur, and C. Meneveau, "Effect of filter type on the statistics of energy transfer between resolved and subfilter scales from a-priori analysis of direct numerical simulations of isotropic turbulence," Journal of Turbulence **19**, 167–197 (2018).

[57]S. Du, H. Li, X. Fu, and Z. Gan, "Anisotropic energy transfer and conversion in magnetized compressible turbulence," The Astrophysical Journal **948**, 72 (2023).

[58]R. S. Strichartz, *A guide to distribution theory and Fourier transforms* (World Scientific Publishing Company, 2003).

[59]L. C. Evans, *Partial Differential Equations* (Amer Mathematical Society, 2010).

[60]A. Leonard, "Energy Cascade in Large-Eddy Simulations of Turbulent Fluid Flows," Adv. Geophys. **18**, A237 (1974).

[61]M. Germano, "Turbulence: the filtering approach," Journal of Fluid Mechanics **238**, 325–336 (1992).

[62]H. Aluie, "Coarse-grained incompressible magnetohydrodynamics: analyzing the turbulent cascades," New Journal of Physics **19**, 025008 (2017).

[63]I. Daubechies, *Ten Lectures on Wavelets* (Society for Industrial and Applied Mathematics, 1992) https://epubs.siam.org/doi/pdf/10.1137/1.9781611970104.

[64]H. Aluie, M. Hecht, and G. K. Vallis, "Mapping the Energy Cascade in the North Atlantic Ocean: The Coarse-graining Approach," Journal of Physical Oceanography **48**, 225–244 (2018), 1710.07963.

[65]D. Zhao and H. Aluie, "Inviscid criterion for decomposing scales ," Physical Review Fluids **3**, 054603 (2018).

[66]B. A. Storer, M. Buzzicotti, H. Khatri, S. M. Griffies, and H. Aluie, "Global energy spectrum of the general oceanic circulation," Nature Communications **13**, 5314 (2022).

[67]P. Chassaing, "An alternative formulation of the equations of turbulent motion for a fluid of variable density," Journal de Mecanique Theorique et Appliquee **4**, 375–389 (1985).

[68]D. J. Bodony and S. K. Lele, "On using large-eddy simulation for the prediction of noise from cold and heated turbulent jets," Physics of Fluids **17**, 085103 (2005), https://doi.org/10.1063/1.2001689.

[69]G. C. Burton, "Study of ultrahigh Atwood-number Rayleigh–Taylor mixing dynamics using the nonlinear large-eddy simulation method," Physics of Fluids **23**, 045106 (2011), https://doi.org/10.1063/1.3549931.

[70]M. Karimi and S. S. Girimaji, "Influence of orientation on the evolution of small perturbations in compressible shear layers with inflection points," Phys. Rev. E **95**, 033112 (2017).

[71]S. Kida and S. A. Orszag, "Energy and spectral dynamics in forced compressible turbulence," Journal of Scientific Computing **5**, 85–125 (1990).

[72]A. W. Cook and Y. Zhou, "Energy transfer in Rayleigh-Taylor instability," Phys. Rev. E **66**, 026312 (2002).

[73]P. Grete, B. W. O'Shea, K. Beckwith, W. Schmidt, and A. Christlieb, "Energy transfer in compressible magnetohydrodynamic turbulence," Physics of Plasmas **24**, 092311 (2017), https://doi.org/10.1063/1.4990613.

[74]D. Zhao and H. Aluie, "Inviscid criterion for decomposing scales," Phys. Rev. Fluids **3**, 054603 (2018).

[75]A. J. Favre, J. J. Gaviglio, and R. J. Dumas, "Further space-time correlations of velocity in a turbulent boundary layer," Journal of Fluid Mechanics **3**, 344–356 (1958).

[76]T. D. Drivas and G. L. Eyink, "An Onsager singularity theorem for turbulent solutions of compressible Euler equations," Communications in Mathematical Physics **359**, 733–763 (2018).

[77]H. Aluie and S. Kurien, "Joint downscale fluxes of energy and potential enstrophy in rotating stratified Boussinesq flows," EPL (Europhysics Letters) **96**, 44006 (2011).

[78]M. Sadek and H. Aluie, "Extracting the spectrum of a flow by spatial filtering," Physical Review Fluids **3**, 124610 (2018).

[79]We note that the 4.1% difference between the two highlighted values in Table III (4.80×10^9 erg/cm^3) and Table IV (4.60×10^9 erg/cm^3) is, at least in part, due to temporal discretization errors when calculating the integrals $\int\Gamma$.*J. O. Hinze, Turbulence (2nd ed.)* (*McGraw – Hill*, 1975).

[80]X. Bian, J. K. Shang, E. G. Blackman, G. W. Collins, and H. Aluie, "Scaling of turbulent viscosity and resistivity: extracting a scale-dependent turbulent magnetic prandtl number," The Astrophysical Journal Letters **917**, L3 (2021).

[82]M. Buzzicotti, B. A. Storer, H. Khatri, S. M. Griffies, and H. Aluie, "Spatio-temporal coarse-graining decomposition of the global ocean geostrophic kinetic energy," Journal of Advances in Modeling Earth Systems (2023), 10.48550/arXiv.2106.04157, 2106.04157.

[83]J. v. Bladel, "On Helmholtz's theorem in finite regions," Wisconsin: Midwestern Universities Research Association (1958).

[84]J. Qian, "Inverse energy cascade in two-dimensional turbulence," The Physics of Fluids **29**, 3608–3611 (1986), https://aip.scitation.org/doi/pdf/10.1063/1.865788.

[85]G. Boffetta and R. E. Ecke, "Two-dimensional turbulence," Annual Review of Fluid Mechanics **44**, 427–451 (2012), https://doi.org/10.1146/annurev-fluid-120710-101240.

[86]H. Aluie, S. Rai, H. Yin, A. Lees, D. Zhao, S. M. Griffies, A. Adcroft, and J. K. Shang, "Effective drift velocity from turbulent transport by vorticity," Phys. Rev. Fluids **7**, 104601 (2022).

APPENDIX

Fig. 20 shows that the average traveling speed converges at refinement level 5, which is chosen for the runtime parameter stated in simulation configurations in Section II A.

Fig. 21 provides two compressibility metrics supplemental to Section II D, where the 2D jet presents higher compressibility levels at the end of the simulation ($t = 3.5$ ns). Fig. 21a is the bulk Mach number that compares the visualization of Mach number in Fig. 9. A difference of 12.1% between 2D and 3D occurs at the end of the simulation ($t = 3.5$ ns). Fig. 21b is the root mean square (rms) ratio of divergence of velocity (Fig. 10a) to curl of velocity (Fig. 10b). The ratios for 2D and 3D are both below one implying the significance of the divergence-free part of the flow even with the strong shock in the domain.

Fig. 22 - 24 compare the coarse-grained fields with two boundary conditions: zero-gradient boundary and mirrored boundary. Fig. 22 visualizes the coarse y-velocity and Fig. 23 visualizes the y-gradient of coarse y-velocity. Fig. 24 compares a lineout for Fig. 22 and Fig. 23, and demonstrates the differences between the two boundary conditions are negligible. The mirrored boundary is selected to be the boundary condition for the simulations described in Section III A.

Fig. 25 shows the evolution of dominant component (y-component) of the kinetic energy at various scales, There is more kinetic energy in 2D at large scales compare to 3D, which is consistent with the evolution of total kinetic energy in Fig. 11.

Fig. 26 provides that, at $t = 3.5$ ns, Π_ℓ transfers energy upscale and Λ_ℓ mainly transfers energy downscale as discussed in Section IV B.

Fig. 27 shows the deformation work and baropycnal work due to the dilatational flow at $t = 3.5$ ns. Energy transfer directions are the same in 2D and 3D for both $\langle \Pi_\ell^{dil} \rangle$ and $\langle \Lambda_\ell^{dil} \rangle$, which follows the dynamics in homogeneous compressible turbulence[42].

Fig. 28 shows the components of deformation work, $\langle \Pi_\ell \rangle$, calculated with cross terms at $t = 3.5$ ns. All components transfer energy downscale in both 2D and 3D, highlighting the contrast of dynamics of $\langle \Pi^{sol} \rangle$ discussed in Section VI A.

Fig. 29 overlaps the coarse vorticity and streamlines to show the correlation between the high-intensity vorticity and the generation of the circulations discussed in Section VI B.

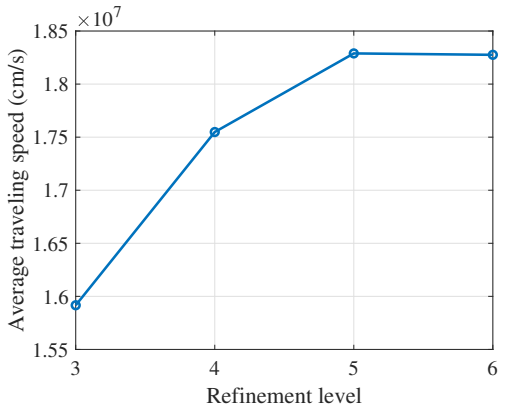

FIG. 20. Convergence study taking average traveling speed (ratio of traveling distance, characterized by $G_y^{centroid}$, to time) at different refinement levels. Average traveling speed converges at refinement level 5.

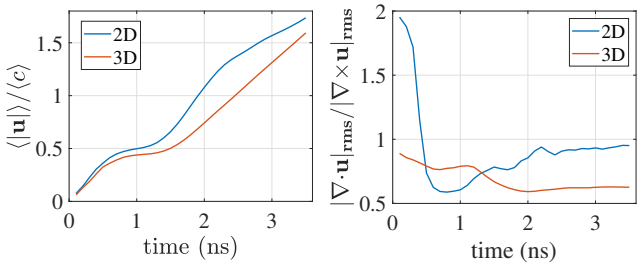

(a) $M = \langle |\mathbf{u}| \rangle / \langle c \rangle$ (b) $|\nabla \cdot \mathbf{u}|_{rms} / |\nabla \times \mathbf{u}|_{rms}$

FIG. 21. Compressibility metrics in (a) bulk Mach number, M, and (b) root mean square (rms) ratio of divergence of velocity to curl of velocity. The compressibility levels in 2D is larger than in 3D at the end of the simulation ($t = 3.5$ ns).

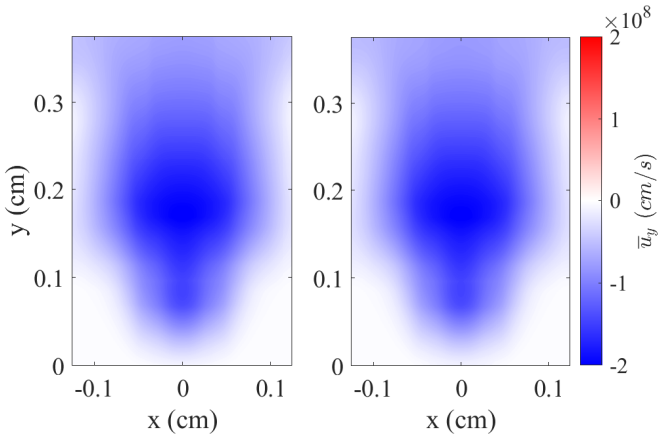

(a) Zero-gradient boundary (b) Mirrored boundary

FIG. 22. Comparing coarse y-velocity, $\overline{u}_y$, with different boundary conditions at $k_\ell = 1$ at $t = 3.5$ ns, where the magnitudes are almost identical.

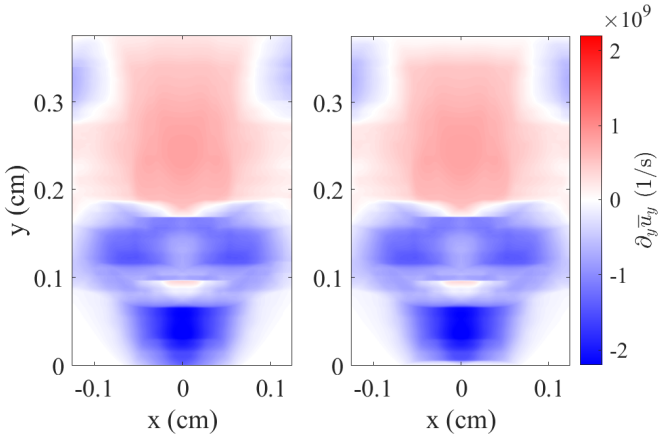

(a) Zero-gradient boundary (b) Mirrored boundary

FIG. 23. Comparing y-gradient of coarse y-velocity, $\partial_y \overline{u}_y$, with different boundary conditions at $k_\ell = 1$ at $t = 3.5$ ns. Compared to Fig. 22, differences are amplified close to the boundaries due to the derivatives.

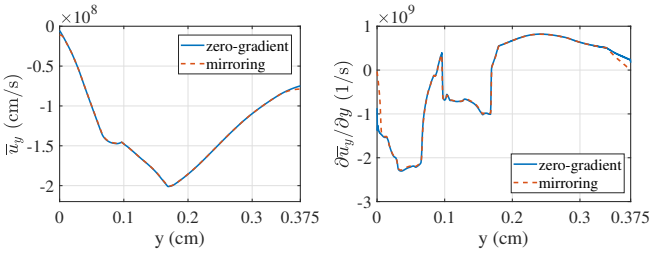

(a) Coarse y-velocity, $\overline{u}_y$ (b) y-component gradient of coarse y-velocity, $\partial_y \overline{u}_y$

FIG. 24. Comparison of zero-gradient and mirrored boundary conditions at $k_\ell = 1$ and $t = 3.5$ ns along the axis $x = 0$ from $y = 0$ to $y = 0.375$ cm. Differences occur near the boundaries and are negligible.

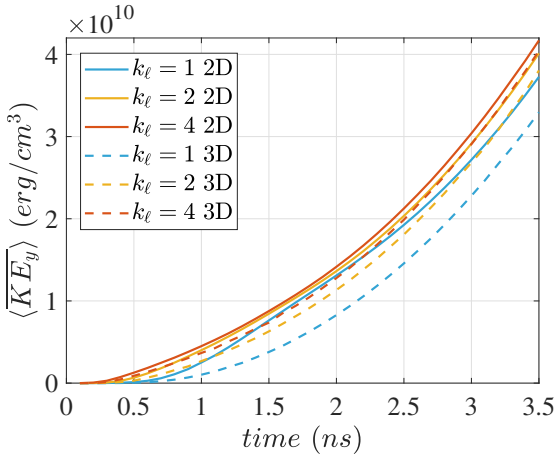

FIG. 25. The y-component of domain-averaged coarse kinetic energy, $\langle \overline{KE_y} \rangle = \langle \rho_\ell \widetilde{u}_{y\ell}^2/2 \rangle$, at all scales $> \ell$. $\langle \overline{KE_y} \rangle$ is the dominant component in total $\langle \overline{KE} \rangle$, and large scales in 2D still possess more KE than in 3D like in Fig. 11.

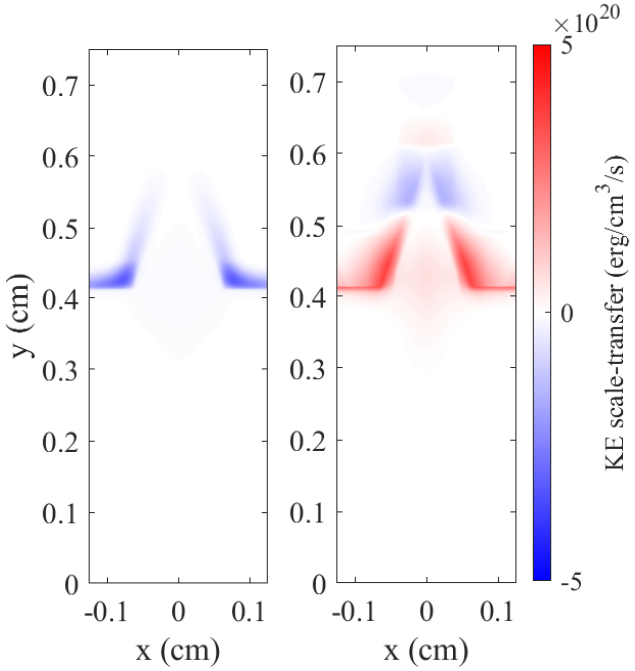

(a) Deformation work, Π_ℓ (b) Baropycnal work, Λ_ℓ

FIG. 26. Visualization of energy scale-transfer by Π_ℓ and Λ_ℓ at $k_\ell = 1$ and $t = 3.5$ ns. Π_ℓ transfers energy upscale and Λ_ℓ mainly transfers energy downscale. Π_ℓ and Λ_ℓ appear localized near the target due to the dominant density contribution.

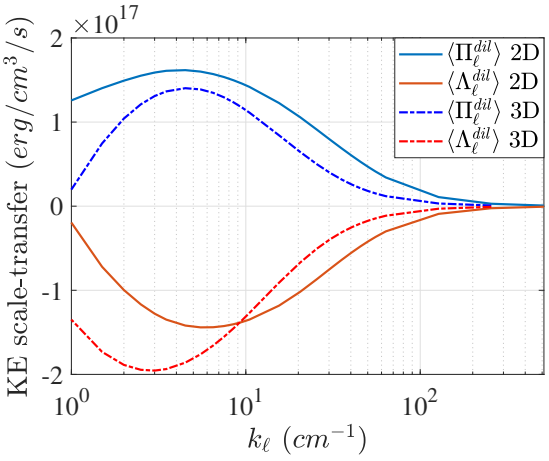

FIG. 27. Deformation work, $\langle \Pi_\ell^{dil} \rangle$, and baropycnal work, $\langle \Lambda_\ell^{dil} \rangle$, due to the dilatational flow and averaged over the subdomain ($y <$ 0.375 cm) highlighted in Fig. 13, plotted here as a function of filtering wavenumber k_ℓ at $t = 3.5$ ns. Energy transfer directions are the same in 2D and 3D for both $\langle \Pi_\ell^{dil} \rangle$ and $\langle \Lambda_\ell^{dil} \rangle$, which follows the dynamics in homogeneous compressible turbulence.

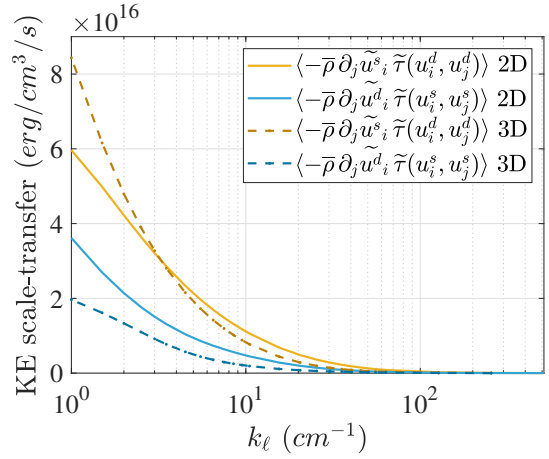

FIG. 28. Components of deformation work, $\langle \Pi_\ell \rangle$, calculated with cross terms and averaged over the subdomain ($y <$ 0.375 cm) highlighted in Fig. 13, plotted here as a function of filtering wavenumber k_ℓ at $t = 3.5$ ns. All components transfer energy downscale in both 2D and 3D, highlighting the contrast of dynamics of $\langle \Pi^{sol} \rangle$ shown in Fig. 16.

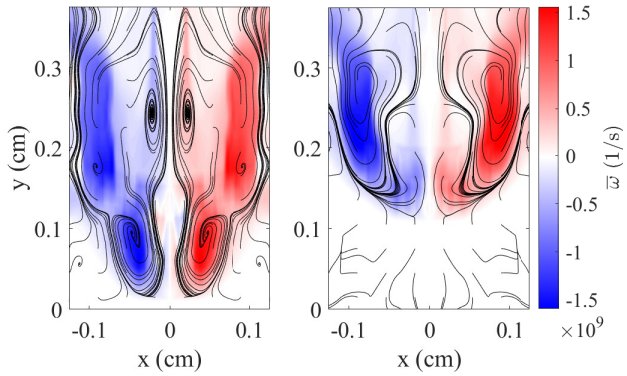

(a) 2D (b) 3D

FIG. 29. Overlapping coarse vorticity $\overline{\omega} = \nabla \times \overline{u}$ and streamlines calculated for the lower half of the domain (y < 0.375 cm) at $t = 3.5$ ns. The $\overline{\omega}$ is at scale $k_\ell = 2$, and the streamlines are generated from the $\tilde{u}$ for the band between $k_\ell = 1$ and $k_\ell = 2$. The overlaps imply the correlation between the high-intensity vorticity and the generation of the circulations.